Tracking vegetation phenology of pristine northern boreal peatlands by combining digital photography with CO₂ flux and remote sensing data

Maiju Linkosalmi[1], Juha-Pekka Tuovinen[1], Olli Nevalainen[1], Mikko Peltoniemi[3], Cemal M. Taniş[2], Ali N. Arslan[2], Juuso Rainne[1], Annalea Lohila[1], Tuomas Laurila[1], Mika Aurela[1]

[1]Finnish Meteorological Institute, Helsinki, Climate System Research, 00560 Helsinki, Finland
[2]Finnish Meteorological Institute, Helsinki, Arctic Space Centre, 00560 Helsinki, Finland
[3]Natural Resources Institute Finland (LUKE), 00790 Helsinki, Finland

Correspondence to: Maiju Linkosalmi (maiju.linkosalm@fmi.fi)

Abstract. Vegetation phenology, which refers to the seasonal changes in plant physiology, biomass and ~~leaf area~~ plant cover, is affected by many abiotic factors, such as precipitation, temperature and water availability. Phenology is also associated with the carbon dioxide (CO_2) exchange between ecosystems and the atmosphere. We employed digital cameras to monitor the vegetation phenology of three northern boreal peatlands during five growing seasons. We derived a greenness index (Green Chromatic Coordinate, GCC) from the images and combined the results with measurements of CO_2 flux, air temperature ~~and water table level,~~ and with high-resolution satellite data (Sentinel-2). From the digital camera images it was possible to extract greenness dynamics on the vegetation community and even species level. The highest GCC and daily maximum gross photosynthetic production (GPP_{max}) were observed at the site with the highest nutrient availability and richest vegetation. The short-term temperature response of GCC depended on temperature and varied among the sites and months. Although the seasonal development and year-to-year variation of GCC and GPP_{max} showed consistent patterns, the short-term variation in GPP_{max} was explained by GCC only during limited periods. GCC clearly indicated the main phases of the growing season, and peatland vegetation showed capability to fully compensate for the impaired growth resulting from a late growing season start. The GCC data derived from Sentinel-2 and digital cameras showed similar seasonal courses, but a reliable timing of different phenological phases depended upon the temporal coverage of satellite data.

1 Introduction

Boreal peatlands constitute a major terrestrial carbon (C) storage and continuously accumulate more C as a result of restricted decomposition of organic matter in anaerobic conditions. Boreal peatlands cover about 3 % of the total land area, but they account for as much as a third of the global C pool (Gorham, 1991; Turunen et al., 2002). Climate and land use changes may disturb the functioning of these ecosystems and affect their exchange of carbon dioxide (CO_2) and other greenhouse gases (GHGs) with the atmosphere. Vegetation phenology, i.e. the seasonal changes in plant physiology, biomass and ~~leaf area~~plant cover (Migliavacca et al., 2011; Sonnentag et al., 2011; Sonnentag et al., 2012; Bauerle et al., 2012), is one of the drivers of the C cycle of terrestrial ecosystems and is strongly linked to plant productivity and CO_2 exchange (Ahrends et al., 2009; Peichl et al., 2015; Toomey et al., 2015; Linkosalmi et al., 2016; Koebsch et al., 2019). Abiotic factors, such as precipitation, temperature, radiation and water availability, act as main drivers of ecosystem functioning and vegetation phenology (Bryant and Baird, 2003; Körner and Basler, 2010). Earlier onset of vegetation growth during the springtime, and thus a longer growing season, has been observed in recent decades in the boreal zone (Linkosalo~~,~~ et al. 2009; Delbart et al., 2008; Nordli et al., 2008; Pudas et al., 2008). This strongly affects the annual C balance of ecosystems, because C accumulation starts as soon as environmental conditions become favourable for

photosynthesis and growth. In contrast, the corresponding lengthening in autumn does not have a similar effect (Goulden et al., 1996; Berninger, 1997; Black et al., 2000; Barr et al., 2007; Richardson et al., 2009), as also ecosystem respiration increases in late summer and autumn (White and Nemani, 2003; Dunn et al., 2007). Even though CO_2 uptake increases due to a longer growing season, natural peatlands have been predicted to lose C as a result of warming and related water table decrease (e.g. Crowther et al., 2016; Harenda et al., 2018). In peatlands, the relationship between greenness and CO_2 exchange has been verified in several studies (Järveoja et al., 2018; Koebsch et al., 2019; Peichl et al., 2015; Peichl et al., 2018; Linkosalmi et al., 2016; Knox et al., 2017). These studies have found a correlation and similar seasonal dynamics between vegetation greenness and CO_2 exchange. Thus, vegetation phenology has been suggested to act as a key driver of the ecosystem-atmosphere CO_2 fluxes.

Remote sensing, both ground- and satellite-based, is an effective tool for continuous monitoring of vegetation greenness and other manifestations of phenology and, thus, indirectly C fluxes. Time-lapse imaging with ground-based digital cameras provides small-scale information on the changes in the vegetation observed, even on the species and vegetation community level. Several studies have shown that such repeat photography is capable of detecting the key patterns and events of vegetation phenology and it is possible to relate these observations to variations in CO_2 exchange (e.g. Wingate et al., 2015; Richardson et al., 2007; Richardson et al., 2009; Linkosalmi et al., 2016; Peichl et al., 2015; Koebsch et al., 2019). Especially, the Green Chromatic Coordinate (GCC) extracted from the red-green-blue (RGB) colour channel information of digital images has been used as an index of canopy greenness (e.g. Richardson et al., 2007; Richardson et al., 2009; Ahrends et al., 2009; Ide et al., 2010; Sonnentag et al., 2012; Peichl et al., 2015; Peltoniemi et al., 2018).

Satellite data offer many benefits for land cover mapping: the data are cost-effective, cover large areas, and even the most remote sites are accessible (e.g. Lees et al., 2018). However, the vegetation and microtopography at many peatland sites are heterogeneous, which complicates the interpretation of satellite data. Furthermore, the presence of both vascular plants and mosses can be challenging for satellite-based monitoring, as the species have different heights and cover each other forming an understory and other vegetation layers. The microtopography depends on the peatland type, and the surface can be relatively flat or patterned with strings and flarks.

In this study, vegetation greennessphenology was observed with digital cameras in three natural peatlands in northern Finland for five growing seasons. Our specific aims were to examine (1) how the GCC describes the variation of vegetation phenology between the sites and among different plant communities within one each site, including the relationship between vegetation phenology and CO_2 flux dynamics, (2) how the abiotic factors (temperature changes, water table depth) modulate the development of GCC and CO_2 flux and (3) the potential use of satellite-derived GCC data for depicting the phenology of northern peatlands.

2 Material and methods

2.1 Sites

The three study sites are natural open peatlands, all located in northern Finland. Halssiaapa in Sodankylä (N67°22.117', E26°39.244', 180 m a.s.l.) is the southernmost of the sites and, as a mesotrophic fen, represents a typical aapa mire. The vegetation mainly consists of sedges (*Carex* spp.*), big-leafed bogbean (*Menyanthes trifoliata*), bog-rosemary (*Andromeda polifolia*), dwarf birch (*Betula nana*), cranberry (*Vaccinium oxycoccos*) and peat moss (*Sphagnum* spp.). Tall trees are not present, only some minor

downy birch (*B. pubescens)* and Scots pine (*Pinus sylvestris)*. Different types of vegetation are located on drier strings (shrubs)

75 and wetter flarks (sedges and herbs). The trophic status varies from oligotrophic to eutrophic.

Lompolojänkkä (N67°59.842', E24°12.569', 269 m a.s.l.) is a nutrient-rich sedge fen located in the Pallas area. Of our study sites, Lompolojänkkä is the richest in nutrients. This is reflected in the vegetation, which is dominated by *B. nana, M.~~enyanthes~~ trifoliata,* downy willow *(Salix lapponum)*, *Carex* spp. and *Sphagnum* and brown mosses (Aurela et al., 2009). Lompolojänkkä has the highest

80 leaf area index among the sites (one-sided LAI of 1.3 m^2 m^{-2}) (Aurela et al., 2009).

Kaamanen (N69°08.435', E27°16.189', 155 m a.s.l.) is the northernmost of the sites and also represents an aapa mire. The site is located within the northern boreal vegetation zone, but the climate is already subarctic (Aurela et al., 1998). Vegetation is distributed to wet flarks and strings of 0.3–0.6 m in height. On the strings, the vegetation mainly consists of ombrotrophic species,

85 such as forest mosses and Ericales (Maanavilja et al., 2011). *Sphagnum* mosses, sedges, *B. nana* and *Andromeda polifolia* dominate the margins of the strings. The flarks are dominated by meso-eutrophic vegetation, such as brown mosses and sedges (Maanavilja et al., 2011). Of these sites, the LAI is lowest (0.7 m^2 m^{-2}) at Kaamanen. At all sites, the snowmelt typically occurs in May.

The monthly mean air temperatures and precipitation sums during the measurement years and their long-term means for the period

90 1981 – 2010 are presented in Supplementary material, Table S1. These data were obtained from the meteorological stations close to the study sites (https://en.ilmatieteenlaitos.fi/download-observations).

2.2 Image analysis

The images were taken with StarDot Netcam SC 5 digital cameras and cover the years from 2015 to 2019. The cameras were placed in a weatherproof housing and attached to line current and a remote web server. Images were taken automatically every 30

95 minutes with a 2592x1944 resolution in 8-bit JPEG format and transferred automatically to the server. The cameras were facing the north and adjusted in a depression angle of 18° at 2 m height at Halssiaapa, of 10° at 3 m at Lompolojänkkä and of 10° at 3.5 m at Kaamanen.~~were adjusted in an angle of 45° on a pole facing the north~~. The cameras were mostly observing the peatland vegetation, but also the skyline was visible in the images. The image quality settings (saturation, contrast and colour balance) were the same ~~in~~ for all cameras.

100

The data gained from the digital camera images consist of colour-based chromatic indices. The images were analyzed with the FMIPROT (version 0.21.1) program that was designed as a toolbox for image processing for phenological and meteorological purposes (Tanis et al., 2018). FMIPROT automatically derives the colour fraction indices from the images. We used the Green Chromatic Coordinate (GCC):

105 $$GCC = \frac{\Sigma G}{\Sigma R + \Sigma G + \Sigma B} \qquad\qquad (1)$$

where ΣG, ΣR, ΣB are the sums of green, red and blue channel indices, respectively, of all pixels comprising an image. In FMIPROT it is possible to choose different subareas, Regions of Interest (ROIs), within the image, for which GCC is calculated separately. At the latitude of our study sites, solar radiation levels have been observed to be sufficient for image analysis from February to October and the diurnal radiation levels acceptable from 11:00 to 15:00 (local winter time, +02:00 GMT) (Linkosalmi et al., 2016).

110 Here, we used images from the beginning of May to the end of September, which represent the growing season, and calculated daily GCC averages ~~were calculated~~ from the images taken during 11:00~~–~~15:00 based on the findings of Linkosalmi et al. (2016).

2.3 Regions of interest (ROIs)

The ROIs covering all ~~different~~ plant communities within the target area of the camera were defined for each site (Fig. 1 a-c). In addition to these general ROIs, more specific ROIs (Fig. 1 d-f) were defined for clearly identifiable plant communities characterized by specific dominant plant species (Table 1).
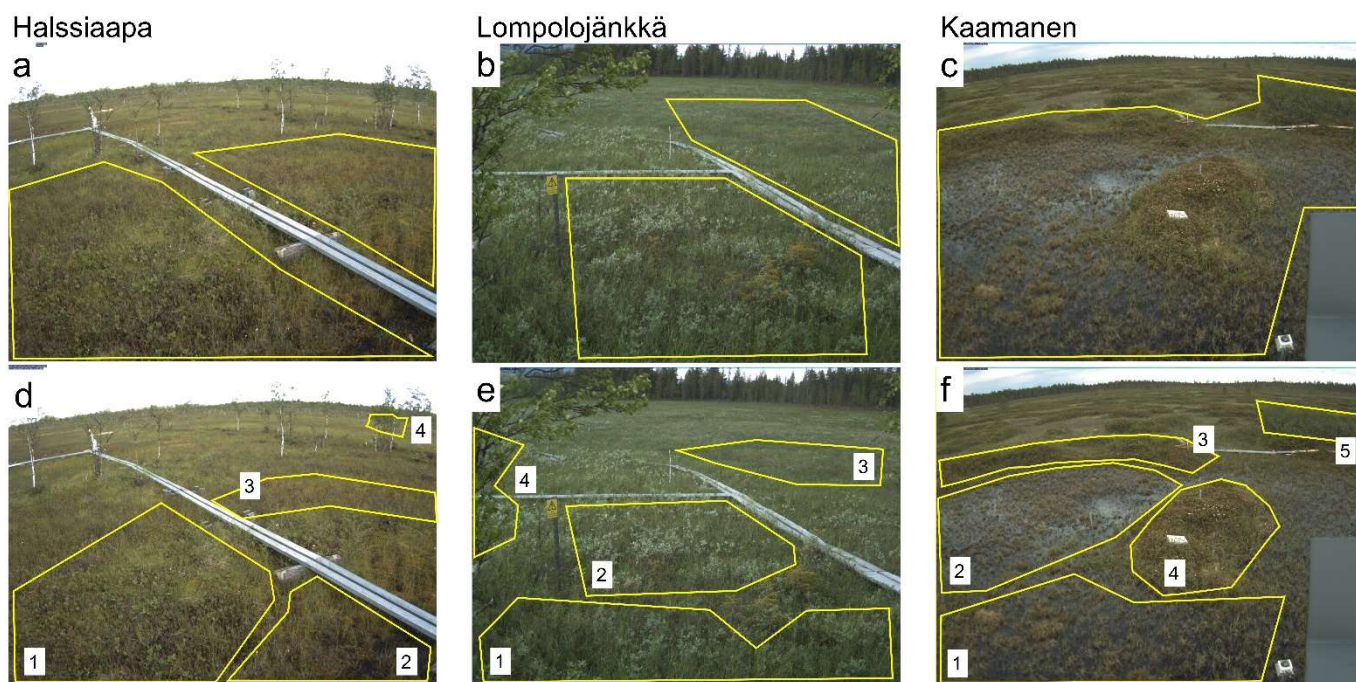
Figure 1: The Region of Interests (ROIs) representing the overall vegetation at the site (a-c) and specific plant communities within the camera target areas (d-f). The numbers 1-5 indicate the plant communities detailed in Table 1.

Table 1: The dominant plant species characterizing the different plant communities within Region of Interests (ROIs) at each site (Fig. 1 d-f).

	Halssiaapa	Lompolojänkkä	Kaamanen
ROI1	*Menyanthes trifoliata*	*Salix* sp., *Carex* spp.	*Carex* spp. and flark mosses
ROI2	Sedges (mostly *Carex* spp.)	*Salix* sp., *Carex* spp.	*Carex* spp. and flark mosses
ROI3	*Andromeda polifolia* and other shrubs	*Carex* spp.	*Empetrum nigrum, Rubus chamaemorus*
ROI4	*Betula pubescens*	*Betula nana*	*Rhododrendron tomentusum, Rubus chamaemorus*
ROI5			*Betula nana*

2.4 Ecosystem scale CO₂ exchange and meteorological observations

The ecosystem–atmosphere CO_2 exchange was measured by the micrometeorological eddy covariance (EC) method. The EC method provides continuous CO_2 flux data averaged ~~on an~~at the ecosystem scale. The vertical CO_2 flux is defined as the covariance

of the high-frequency (10 Hz) fluctuations of vertical wind speed and CO_2 mixing ratio. At each site, the EC measurement system consisted of a USA-1 (METEK GmbH, Elmshorn, Germany) three-axis sonic anemometer and a closed-path LI-7000 (Li-Cor., Inc., Lincoln, NE, USA) CO_2/H_2O gas analyzer. Air temperature, photosynthetic photon flux density (PPFD) and water table level (WTD) were also measured at the sites. The measurement system and the data processing procedures have been presented in detail by Aurela et al. (2009).

The measured CO_2 flux represents the net ecosystem exchange (NEE), which is the sum of gross photosynthetic production (GPP) and ecosystem respiration. The daily maximum GPP, GPP_{max}, was calculated as the difference between the mean daytime (PPFD > 600 µmol m^{-2} s^{-1}) and nighttime (PPFD < 20 µmol m^{-2} s^{-1}) NEE. The GPP_{max} describes the seasonal GPP cycle and also reacts to short-term changes in air temperature and humidity (Aurela et al., 2001).

2.5 Growing degree day sum, growing season start and temperature classes

Growing Degree Day Sum (GDDS) was defined as the cumulative sum of the daily average temperatures exceeding 5 °C, each subtracted with the base value of 5 °C. The thermal growing season was considered to start when the daily mean temperature has remained over 5 °C for ten days, as defined by the Finnish Meteorological Institute (e.g. Lehtonen and Pirinen 2019). The short-term change in GCC was expressed as a mean three-day difference, i.e. $\Delta GCC = GCC(day_t) - GCC(day_{t+3})$. A two-day average of these differences It was calculated for each month during throughout the five growing seasons, and its monthly average wasthese averages were divided into three temperature classes (<5 °C, 5-10 °C and >10 °C) calculated as a two-day average (day$_t$ and day$_{t+1}$). Also, cumulative GCC was calculated using the value observed just before the increase as the baseline growing season start as the baseline. The cumulative sums were normalized by the maximum and minimum values of the year with the maximum cumulative GCC.

2.6 Satellite data

The GCC derived from the digital images of the ground-based cameras was compared with those derived from the Sentinel-2 data acquired from 2016 to 2019. GCC was computed from the atmospherically corrected bottom-of-atmosphere products (Level-2A) using bands B2 (blue, 490 nm), B3 (green, 560 nm) and B4 (red, 665 nm) with a 10 m spatial resolution. The Level-2A products were downloaded from the Sentinel Scientific Data Hub (https://scihub.copernicus.eu). If the Level-2A product was not available for a specific date, the Level-1C product was downloaded and processed to Level-2A product using the Sen2Cor software (version 2.8). Cloudy, cloud-shadowed and snowy satellite images were filtered and discarded using the scene classification data (SCL Band) available in the Level-2A products.

GCC was calculated for multiple ROIs within each site (Fig. 2). These ROIs were different from those used with camera data because of the different spatial resolutions of the camera and satellite data. The selected ROIs represent different vegetation types with different microtopography within the study areas. The average of pixel-based GCCs within a ROI was used as the ROI-based GCC. Site-based GCC was then calculated as the average of all ROI-based GCCs within the site. The Sentinel-2 images were available at the minimum for every two days, due to considerable overlap between satellite orbits at the high latitudes of our study sites.but the f Filtering out the cloud- and snow-contaminated data, however, reduced the number of valid images, which were typically available every 5 to 10 days.
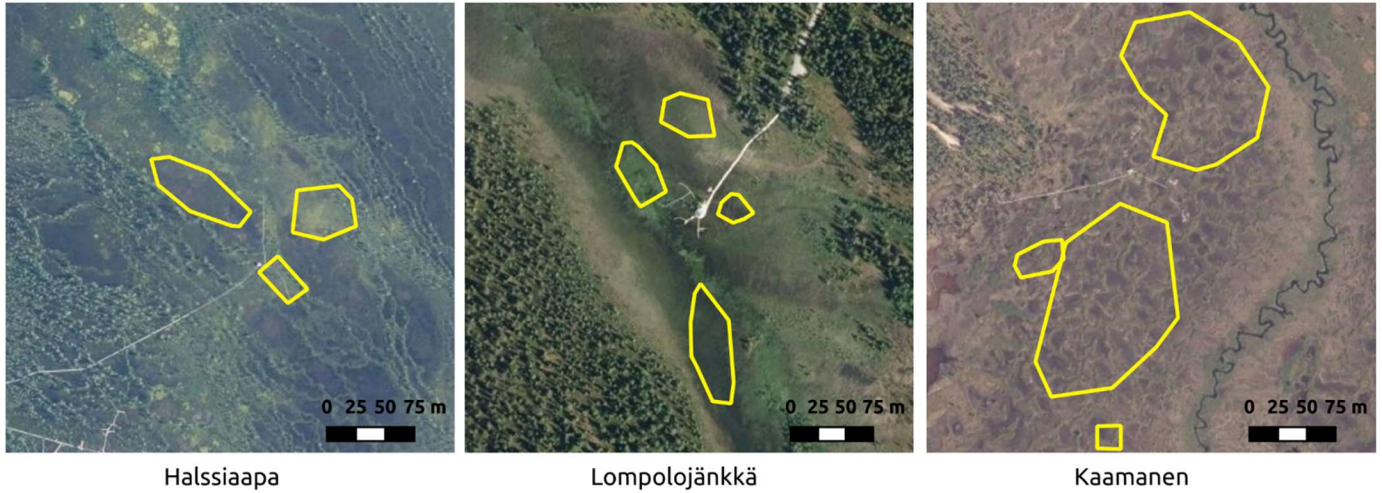
165

Figure 2: The Region of Interests (ROIs) representing the overall vegetation at the sites for the Sentinel-2 satellite images. The aerial photo contains data from the National Land Survey of Finland Topographic Database.

2.7 Fitting of GCC and GPPmax cycles

170   To depict the phenology-driven seasonal cycle, we fitted a double hyperbolic tangent function to both camera- and satellite-derived GCC time series with the Levenberg-Marquardt least squares method (Meroni et al., 2014; Vrieling et al., 2018):

$$GCC(t) = a_0 + a_1 \frac{tanh\ ((t-a_2)a_3)+1}{2} + a_4 \frac{tan\ ((t-a_5)a_6)+1}{2} - a_4, \qquad (2)$$

where t is time, a_0 is the minimum GCC value at the start of the growing season, a_1 (a_4) is the difference between the maximum GCC and minimum GCC, a_2 (a_5) is the inflection point in GCC development, and a_3 (a_6) controls the slope at the inflection point

175   in GCC development during the first (second) half of the growing season. A similar function was fitted to the GPP_{max} data.

Visible snow included in the images affects the GCC data by overexposure. Thus, only the data collected after the snowmelt, which usually occurs in May at all sites, was used. Also, the starting point of the fits was fixed to 1 May (Day of Year (DOY) 121), and the GCC value for this day was calculated as the average of the yearly minima after the snowmelt, whose timing was specified for

180   each year and site. Likewise, the growing season ends by the end of October, and thus the end point of the fit was fixed to 31 October (DOY 304), for which GCC was determined by averaging the annual minima in the end of the growing season.

From the fitted function, we calculated parameters that describe phenological phases and vegetation development. These parameters were chosen as the start of season (SOS25), which stands for 25 % of the GCC difference between the maximum and

185   1 May, maximum GCC (MAX) and the end of season (EOS25), defined as 25 % of the GCC difference between 30 October and the maximum. The thresholds are in accordance with Richardson et al. (2019) and were chosen to minimize the disturbance of excess surface water after the snowmelt.

2.8 Statistical analysis

The differences in GCC between the sites, different plant communities and measurement years were tested with the Kruskal-Wallis

190   one-way analysis of variance on ranks for the group-wise comparison. Dunn's test was used for post-hoc testing and the significance values were adjusted by the Holm correction for multiple tests. The Kruskal-Wallis method was used due to the non-

normal distribution of the seasonal GCC data. The presence of autocorrelation in the residuals of the regression between GCC and GPP$_{max}$ was verified with the Durbin-Watson test. Autocorrelation was eliminated by regressing the first differences of the data, i.e. by applying the transformation $x'_t = x_t - x_{t-1}$ where x_t and x_{t-1} are consecutive observations. The statistical analyses were performed with the R software (version 4.2.00.5).

3 Results

3.1 Greenness variation

The seasonal development of vegetation during the growing season could be visually observed from the imagery collected at our study sites, as exemplified by Figure 3. The spring development, greening and senescence of vegetation during the growing season were visible in the images, and so were the changes in the areas covered by surface water.
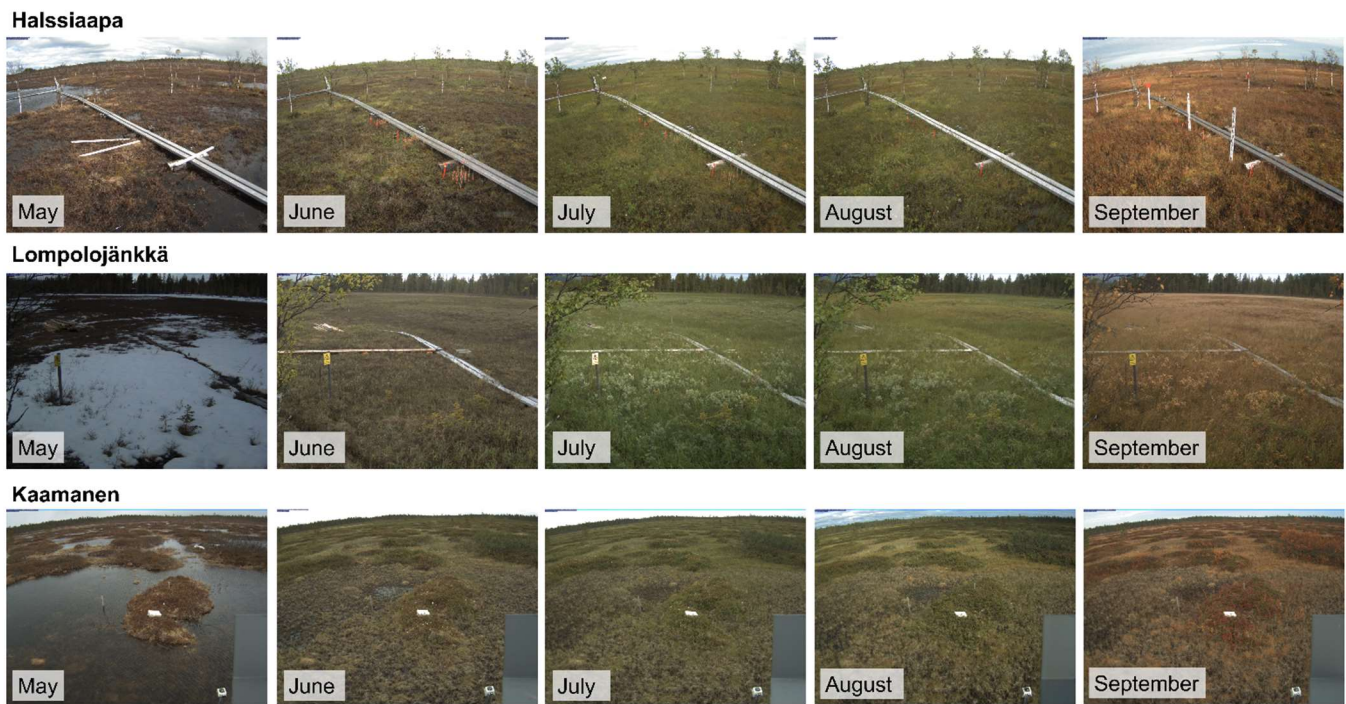
Figure 3: The seasonal development of vegetation and surface water from May to September in 2015 at Halssiaapa, Lompolojänkkä and Kaamanen. The pictures were taken on the 15th of each month, with the exception of the 17th of June at Kaamanen due to missing .

The mean growing season GCC values obtained from the phenological cameras showed that Lompolojänkkä systematically had the highest GCC values over the five growing seasons (Fig. 4 and Supplementary materialAppendices Fig. A4S4, S5 and S6). Kruskal-Wallis groupwise statistical test showed significant difference between the sites during all the measurement years (Table 2). In 2015, 2016 and 20186, there was a significant difference (p < 0.05) in GCC between Lompolojänkkä and the other two sites according to the pairwise statistical analysis (Supplementary material Table S2). In 2017, 2018 and 2019, the pairwise comparison showed a significant (p < 0.05) difference in GCC between Halssiaapa and the other two sitesall the sites (Supplementary material Table S2). The maximum GCC during the whole study period of 2015–2019 was observed in 2017 at Lompolojänkkä and Kaamanen and in 2016 at Halssiaapa (Fig. 4, Table 32).

215
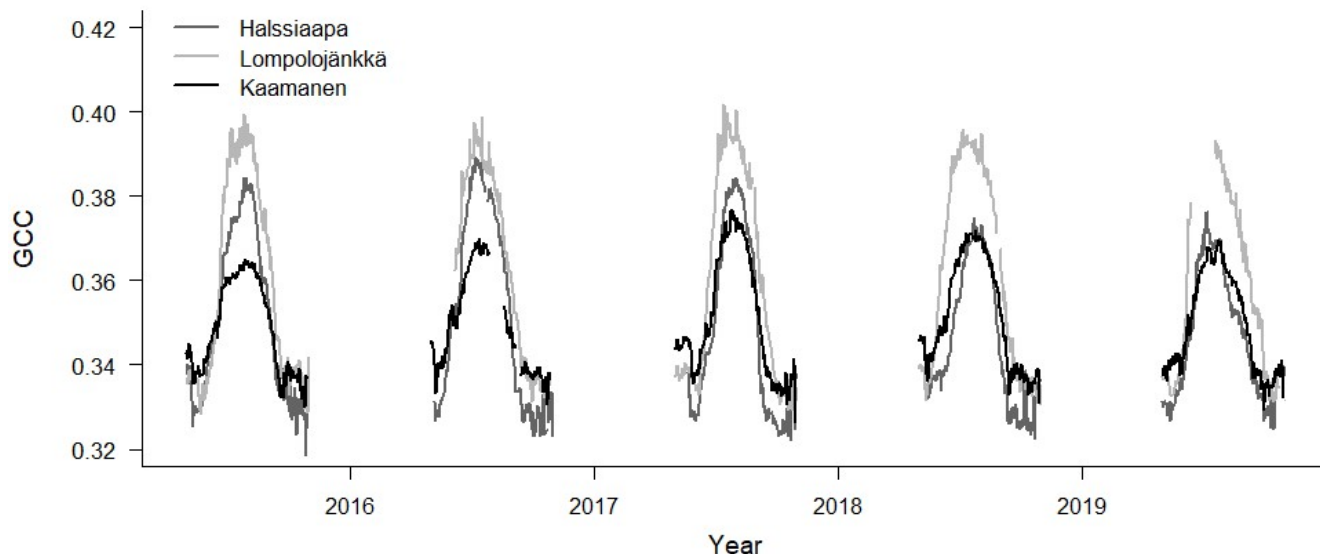
Figure 4: Daily camera-based GCC values from 1 May to 30 September in 2015–2019.

Table 2. The significant differences in GCC between the sites during the measurement years as groupwise comparison
220 **(Kruskal-Wallis one-way analysis of variance on ranks). χ^2 denotes the chi-squared test statistic.**

Year	χ^2	p-value
2015	13.08	1.45×10^{3}
2016	40.27	1.80×10^{9}
2017	25.00	3.72×10^{6}
2018	48.34	3.19×10^{11}
2019	18.74	8.54×10^{5}

Table 32: The mean GCC and GPP$_{max}$ (mg CO$_2$ m^{-2} s^{-1}) during the week they attained the maximum, the week numbers of these maxima and the week number of the growing season (GS) start. The maximum GCC and GPP$_{max}$, the earliest
225 **maximum GCC and GPP$_{max}$ and the earliest GS start are marked as bold. The maximum GCC data from at Lompolojänkkä and maximum GPP$_{max}$ data from at Kaamanen are not reported for from 2019 are missingdue to data gaps.**

Halssiaapa

	Max GCC	Max GCC week	Max GPP$_{max}$	Max GP week	GS start week
2015	0.383 ± 0.018	31	0.318 ± 0.097	30	22
2016	**0.388 ± 0.022**	**27**	**0.353 ± 0.108**	**27**	**18**
2017	0.383 ± 0.020	31	0.338 ± 0.123	32	23
2018	0.371 ± 0.016	29	0.257 ± 0.090	32	19
2019	0.372 ± 0.015	**27**	0.302 ± 0.073	28	21

Lompolojänkkä

	Max GCC	Max GCC week	Max GPP$_{max}$	Max GP week	GS start week
2015	0.396 ± 0.024	31	0.520 ± 0.184	31	22
2016	0.394 ± 0.020	**27**	0.551 ± 0.185	**27**	20
2017	**0.397 ± 0.024**	29	**0.563 ± 0.209**	31	23
2018	0.394 ± 0.022	**27**	0.498 ± 0.181	30	**19**
2019	-	-	0.555 ± 0.197	29	22

Kaamanen

	Max GCC	Max GCC week	Max GPP$_{max}$	Max GP week	GS start week
2015	0.364 ± 0.010	31	0.299 ± 0.094	30	22
2016	0.368 ± 0.011	**29**	0.297 ± 0.089	**28**	**19**
2017	**0.376 ± 0.014**	30	**0.335 ± 0.116**	29	23
2018	0.371 ± 0.012	**29**	0.261 ± 0.090	32	**19**
2019	0.369 ± 0.012	30	-	-	22

230

There were significant GCC differences among different plant communities at all sites (p < 0.05), except in 2017 at Halssiaapa and Kaamanen (Supplementary material~~Appendices~~ Table ~~A1~~S3 and S4). In general, at all sites the GCC of birch species (*Betula pubescens* and *B. nana*) differed significantly from the other plant species. At Halssiaapa, the plant communities with sedges (*Carex* spp.) and shrubs (e.g. *Andromeda polifolia*) differed from annuals with bigger leaves, such as *Menyanthes trifoliata*. At

235 Kaamanen, the shrubs and annuals (e.g. *Empetrum nigrum*, *Rhododendron tomentusum*, *Rubus chamaemorus*) had a significantly higher GCC than the plant communities with sedges and flark mosses. The comparison of the maximum GCC values of different plant communities, calculated as weekly means, supported these results as the annuals and woody plants with relatively large leaves, such as *M.~~enyanthes~~ trifoliata*, *R.~~ubus~~ chamaemorus*, *Salix* spp. and *Betula* spp., generated a higher GCC maximum than *Carex* spp. and shrubs (Table ~~3~~4). At Halssiaapa, the highest maximum GCC during 2015–2017 and 2019 was observed in ROI1,

240 which is dominated by *M.~~enyanthes~~ trifoliata*, whereas in 2018 the highest GCC was found for ROI3, an area with *A.~~ndromeda~~ polifolia* and other shrubs. At Lompolojänkkä, the highest annual GCC maximum was consistently observed in a plant community dominated by *Salix* sp. and *Carex* spp~~.~~ (ROI1). Most likely the ground layer with mosses and dead plant material reduced the GCC within those ROIs that had sparse vegetation. Among the measurement years, most plant communities at Halssiaapa showed the highest maximum GCC in 2016. At Lompolojänkkä, the maximum GCC of different ROIs varied between the years 2015, 2016

245 and 2017, while at Kaamanen all plant communities attained their maxima in 2017.

Table ~~3~~4: The maximum GCC values of different plant communities characterized by the dominant species specified in Table 1 (defined as image ROIs) from 2015 to 2019. The maximum value among different ROIs is marked as bold, and the maximum among the years is underlined. The ROIs are described in Section 2.4. The data from Lompolojänkkä are missing

250 **in 2019.**

Halssiaapa

	ROI1	ROI2	ROI3	ROI4
2015	**0.387 ± 0.019**	0.373 ± 0.016	0.376 ± 0.018	0.372 ± 0.016
2016	**0.391 ± 0.023**	0.378 ± 0.019	0.382 ± 0.021	0.371 ± 0.015
2017	**0.384 ± 0.020**	0.358 ± 0.018	0.381 ± 0.021	0.372 ± 0.016
2018	0.370 ± 0.015	0.365 ± 0.014	**0.374 ± 0.018**	0.370 ± 0.013
2019	**0.374 ± 0.015**	0.366 ± 0.013	0.368 ± 0.014	0.371 ± 0.013

Lompolojänkkä

	ROI1	ROI2	ROI3	ROI4
2015	**0.406 ± 0.027**	0.395 ± 0.024	0.388 ± 0.022	0.403 ± 0.026
2016	**0.400 ± 0.019**	0.393 ± 0.022	0.396 ± 0.021	0.397 ± 0.024
2017	**0.406 ± 0.027**	0.393 ± 0.023	0.396 ± 0.023	0.402 ± 0.027
2018	**0.401 ± 0.023**	0.392 ± 0.022	0.393 ± 0.022	0.400 ± 0.024
2019	-	-	-	-

Kaamanen

	ROI1	ROI2	ROI3	ROI4	ROI5
2015	0.358 ± 0.008	0.357 ± 0.007	**0.376 ± 0.016**	0.375 ± 0.016	0.374 ± 0.019
2016	0.363 ± 0.009	0.362 ± 0.008	**0.380 ± 0.016**	0.379 ± 0.016	0.377 ± 0.017
2017	0.371 ± 0.011	0.368 ± 0.010	0.384 ± 0.019	**0.388 ± 0.021**	0.385 ± 0.019
2018	0.365 ± 0.009	0.365 ± 0.009	0.379 ± 0.015	**0.381 ± 0.017**	0.378 ± 0.016
2019	0.363 ± 0.008	0.362 ± 0.007	**0.379 ± 0.015**	0.377 ± 0.015	0.378 ± 0.016

3.2 Temperature and GCC development

The relationship between temperature and GCC was examined by creating normalized cumulative GCC and GDDS curves for all the growing seasons (Supplementary materialAppendices Fig. A4S4, S5 and S6). These cumulative sums show that the GCC started to accumulate later than GDDS. In 2017, the snow cover lasted at all sites until the beginning of June, which delayed the GDDS development and the start of the growing season compared to the other study years (Figs. 5, and 7, 8 and 9 and Supplementary materialAppendices Figs. A3 S3 and A4S4, S5 and S6). Consequently, GCC did not increase until the beginning of June (4 June in Halssiaapa and Lompolojänkkä and 7 June in Kaamanen), when the snow was melted. Despite the slow start of growth in 2017, the peatland vegetation was capable of catching up its typical development, and at Lompolojänkkä and Kaamanen GCC even reached the highest summer maximum during the study years (Table 23).

During the measurement years, warmer springs and thus earlier snowmelts resulted in an earlier green-up of vegetation. No clear connection between the growing season start and the timing of the maximum of either GCC or GPP$_{max}$ was found at Lompolojänkkä or Kaamanen (Table 23). At Halssiaapa, however, the earliest growing season start, the maximum value and the earliest timing of both GCC and GPP$_{max}$ occurred in the same year, 2016. During our study period, the year 2018 had the warmest summer at all sites (Supplementary material Fig. S3). July 2018 had the highest mean air temperature among the measurement years, which was also higher than the mean temperature of the period 1981–2010 (Supplementary material Table S1). The high temperatures and low precipitation resulted in drought, which was observed as a WTD drop at Halssiaapa and Kaamanen (Supplementary materialAppendices Figs. AS2 & A3 and Table S1). June 2018 was average in terms of meteorological conditions, but the mean air temperatures during the measurement years were highest in 2018 (Supplementary material Table S1). At Halssiaapa, the water

table depthWTD increased substantially during the growing seasons of 2018 and similarly in 2019 as a result of the drought (Supplementary materialAppendices Fig. A2S2). The same was true at Kaamanen (data missing in 2019), while at Lompolojänkkä WTD was not affected. The effect of drought is also visible in the daily and cumulative GCC values (Fig. 4 and Supplementary materialAppendices Fig. A4S4, S5 and S6).
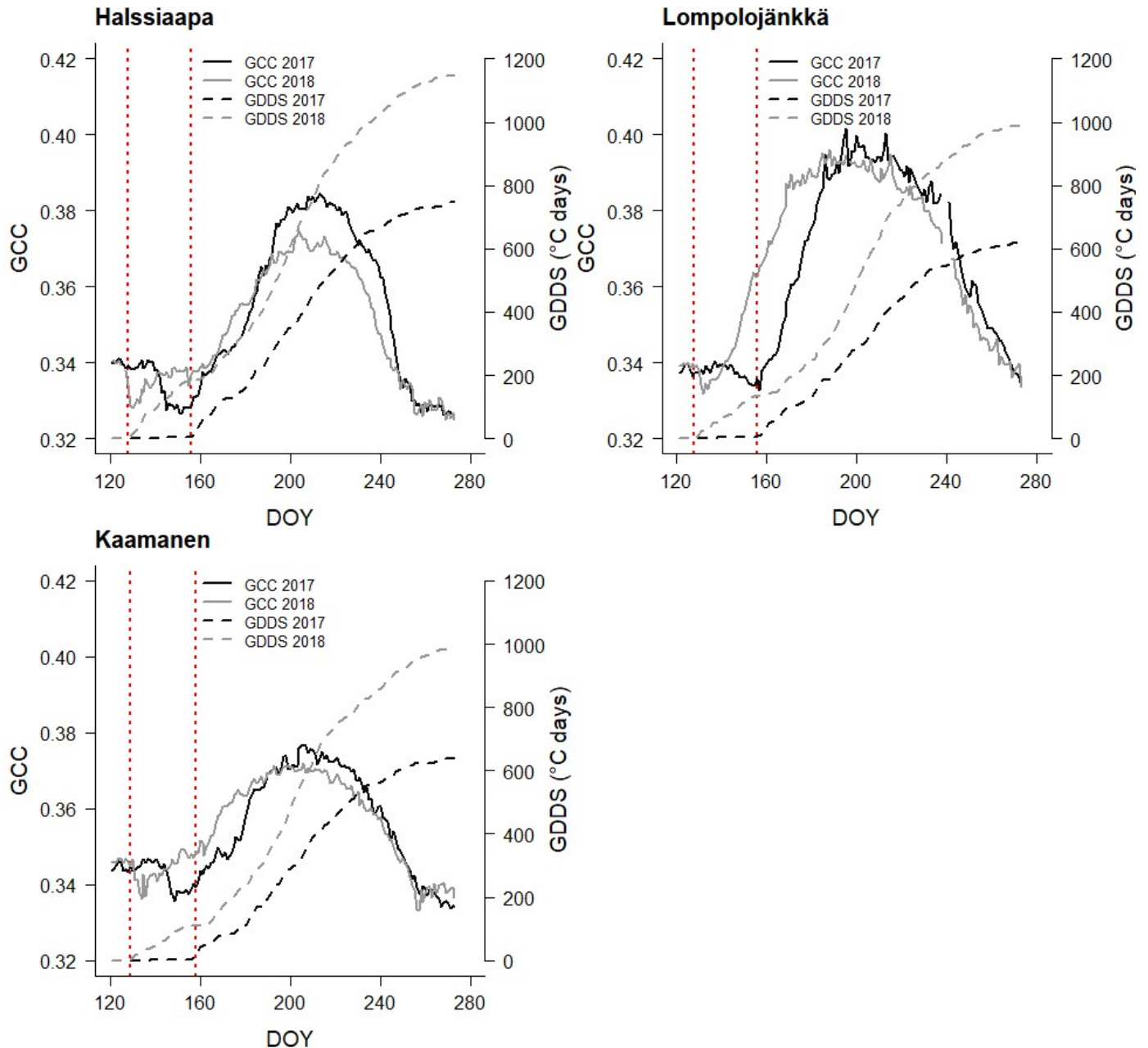
Figure 5: Development of GCC and growing degree day sum (GDDS) from 1 May to 30 September at Halssiaapa, Lompolojänkkä and Kaamanen. The years 2017 and 2018 are shown here as an example of a cold and warm spring, respectively. The grey dashed lines indicate the start of the growing season.

The short-term (3-day) change in GCC change, ΔGCC, which is indicative of vegetation development in different temperature classesexpressed here as the monthly mean 3-day difference, depended on both the month and temperature range (Fig. 6). In May, ΔGCCthis change, which is indicative of vegetation development, was substantially smaller for temperatures below 5 °C, than above 5 °C. No significant (p < 0.05) differences were found between the sites, nor during any month, in the lowest temperature

class (Fig. 6, Supplementary material Table S5). At Lompolojänkkä, ΔGCC started at a lower temperature and was generally larger than at the other sites. The vegetation growth in June at Halssiaapa seemed to benefit from temperatures over 10 °C, while at Lompolojänkkä this limit was lower. At Kaamanen, however, the ΔGCC in June was similar in all temperature classes. In July, GCC started to stabilize and a significant positive change was only observed at Kaamanen for temperatures between 5 and 10 °C and at Halssiaapa with for temperatures over 10 °C. In August and September, ΔGCC was negative due to senescence (Fig. 6). The results of statistical pairwise comparisons and significant differences between the sites are shown in Supplementary material Table S6.

The ΔGCC of different plant communities (Supplementary materialAppendices Fig. A5S7, S8 and S9) showed that the growth of *Betula* spp. started strong in May at all sites, but in June the birches already had a lower ΔGCC than other plant communities. The highest plant community-specific ΔGCC values were found at Lompolojänkkä, which was consistent with the spatially averaged ΔGCC data (Figs. 4 & and 6).
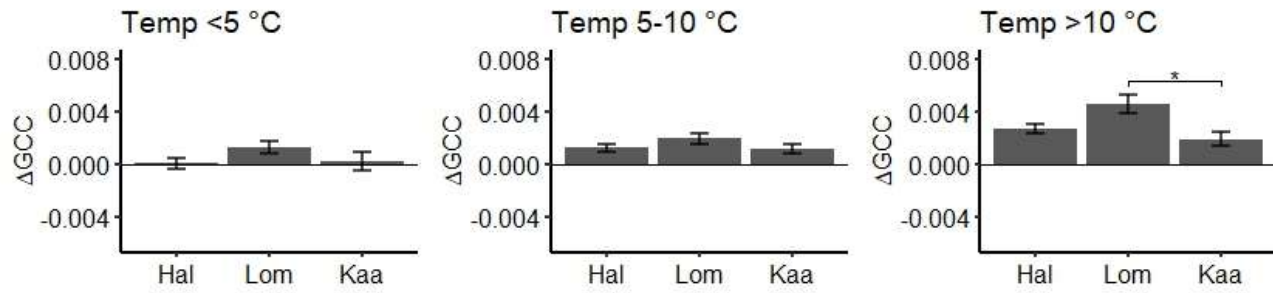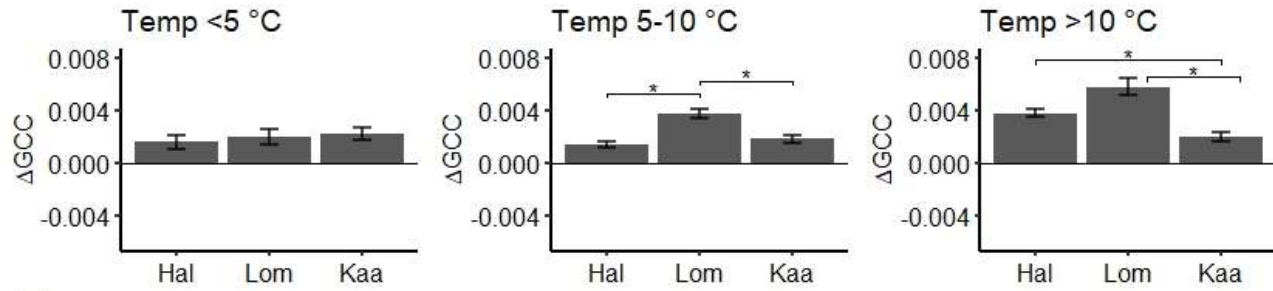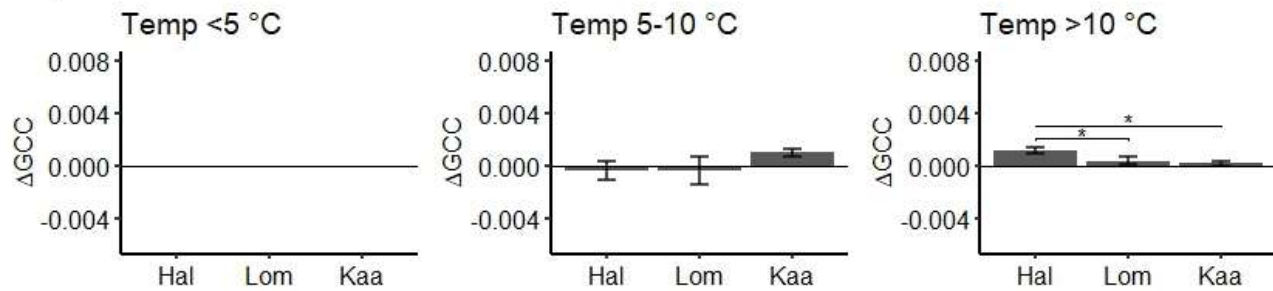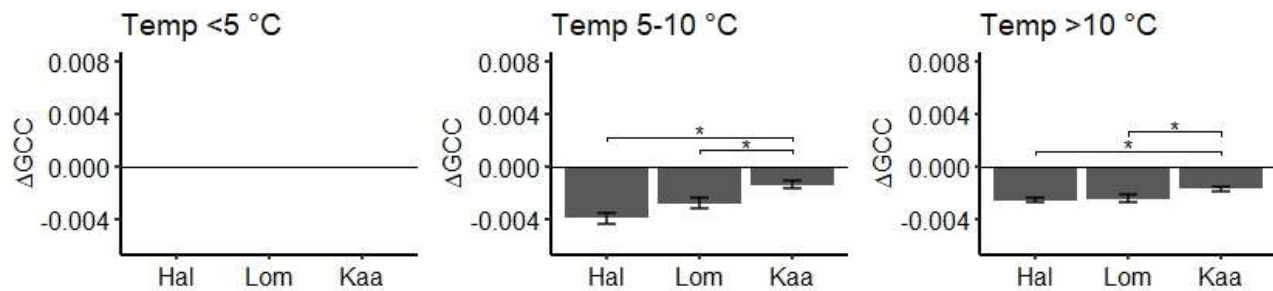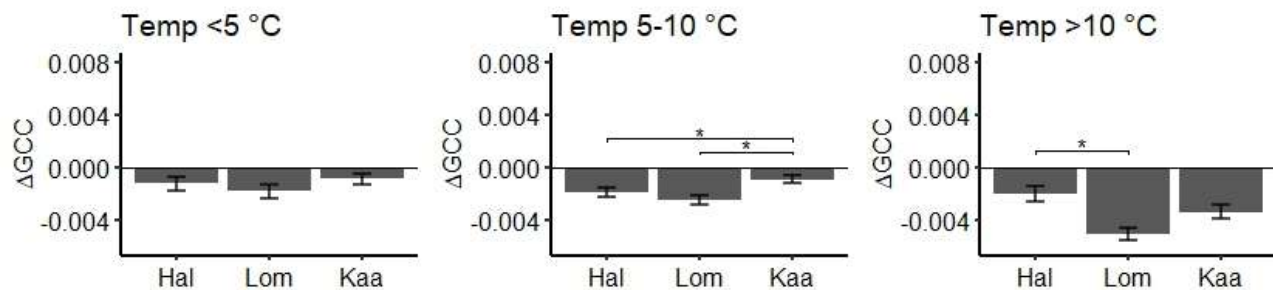
300   **Figure 6: Mean three-day difference in GCC divided to temperature classes (<5 °C, 5–10 °C, >10 °C) at Halssiaapa (Hal), Lompolojänkkä (Lom) and Kaamanen (Kaa) from May to September. There are no temperature data in the <5 °C class in July and August. The error bars denote the standard error, and the asterisks denote the statistically significant (p < 0.05) difference between the sites.**

3.3 Seasonal GCC and GPPmax development

305 The start and end of the growing season were clearly visible in both the GCC and GPP$_{max}$ data, which showed the same seasonal pattern (Fig~~s~~. 7, 8 and 9 ~~& 8~~). As mentioned above, in 2017 the snow cover lasted until the beginning of June, which delayed the start of photosynthesis and thus vegetation development. At Halssiaapa, the year 2018 was hot and dry compared to the other measurement years and the long-term average (Supplementary material~~Appendices~~ Fig. ~~A2~~S2 and Table S1), and this was reflected in the GCC and GPP$_{max}$ data that were lower than in other years (Fig. 7 ~~& 8~~). In addition, t~~T~~he GPP$_{max}$ data were sparse during the

310 growing season of 2018 at Halssiaapa, which impaired the fit and resulted in a wider confidence interval (Fig. 7~~8~~). During the study period, the highest values of both GCC and GPP$_{max}$ were observed in 2016 at Halssiaapa and in 2017 at Kaamanen and Lompolojänkkä (Fig~~s~~. 7, 8 and 9 ~~& 8~~). In general, Lompolojänkkä had the highest GPP$_{max}$, GCC and LAI (Figs. 4 and~~,~~ 7, 8 and 9 ~~and 8~~).

315 The difference in GCC was significant (p < 0.05) between Lompolojänkkä and the other two sites in 2015, 2016 and 2018~~in all years~~ (Supplementary material Table S2). The difference in GCC between Halssiaapa and other sites was significant~~, and~~ in years 2017, 2018 and 2019 ~~also between Halssiaapa and Kaamanen~~(Supplementary material Table S2). In 201~~7~~5, GPP$_{max}$ showed no statistical difference among the sites (Supplementary material Table S7).~~, but i~~ In 2016 and 2019 there was a significant difference (p < 0.05) between Kaamanen and the other two sites, and in 201~~5~~7 and 2018 between Lompolojänkkä and Kaamanen

320 (Supplementary material Table S8). The GPP$_{max}$ and GCC showed a similar course throughout the growing season (Supplementary material~~Appendices~~ Fig. ~~A9~~S19, S20 and S21).
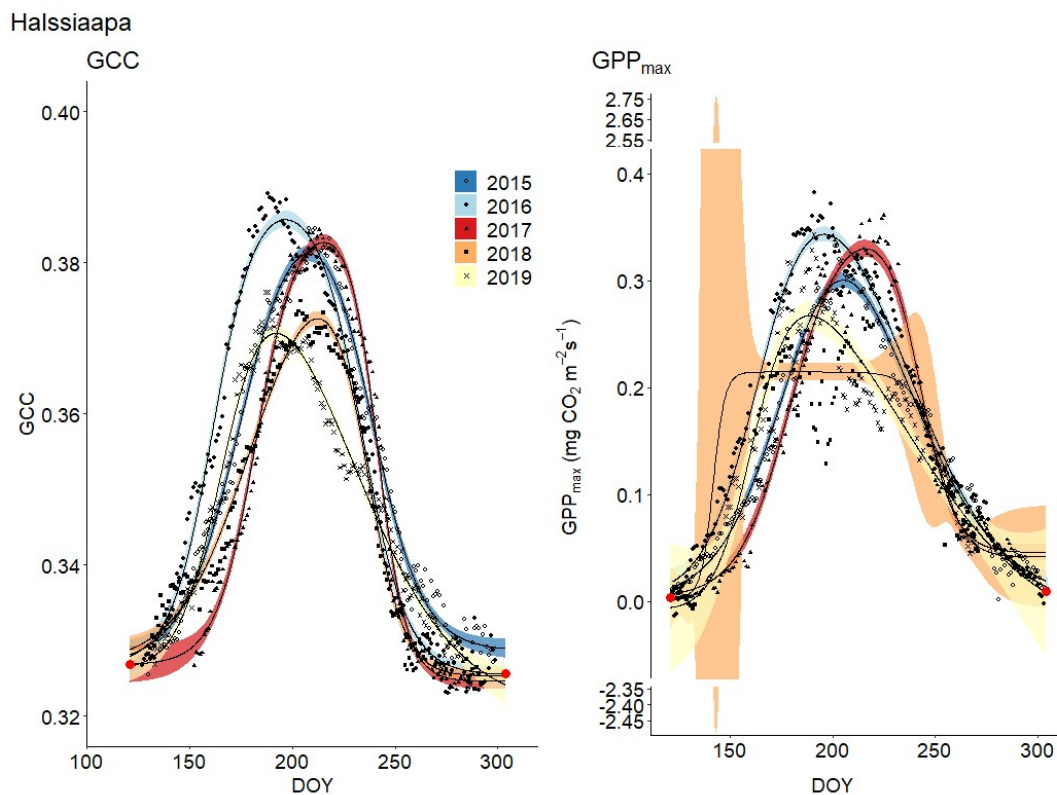
324 **Figure 7: Development of GCC and GPP$_{max}$ from 1 May to 30 September in 2015–2019 at Halssiaapa. Different symbols**
325 **and colours denote different years, and the bands show the 95 % confidence intervals of the fitted double hyperbolic tangent function. The red dots indicate the fixed start and end days defined for the fitting.**

Lompolojänkkä
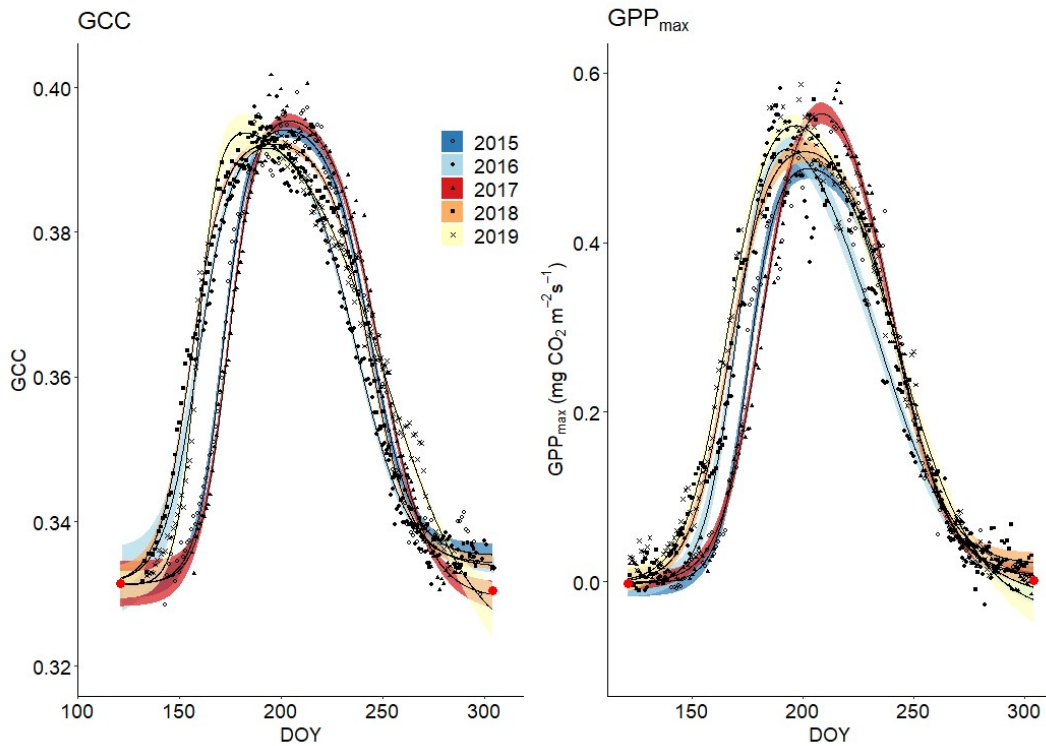
Figure 8: Development of GCC and GPP$_{max}$ from 1 May to 30 September in 2015–2019 at Lompolojänkkä. Different symbols and colours denote different years, and the bands show the 95 % confidence intervals of the fitted double hyperbolic tangent function. The red dots indicate the fixed start and end days defined for the fitting.

Kaamanen
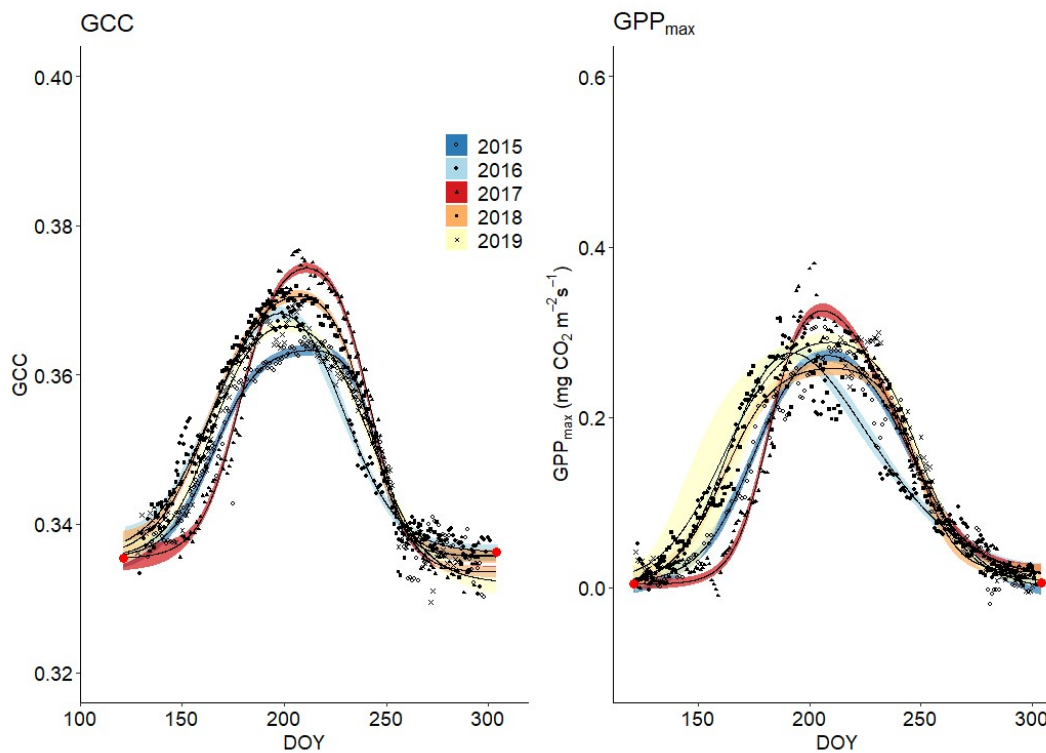
Figure 9: Development of GCC and GPP$_{max}$ from 1 May to 30 September in 2015–2019 at Kaamanen. Different symbols and colours denote different years, and the bands show the 95 % confidence intervals of the fitted double hyperbolic tangent function. The red dots indicate the fixed start and end days defined for the fitting.

A linear relationship between GCC and GPP_{max} was observed during both the increasing and decreasing phases of GCC (Table 45, Supplementary materialAppendices Fig. A8S16, S17 and S18). The coefficient of determination (R^2) of the original linear regression for the first phase of 2018 at Halssiaapa was low due to a gap in the GPP_{max} data and the hot and dry weather conditions that temporarily reduced GPP_{max}. However, the Durbin-Watson test indicated that there was significant and strong autocorrelation in the model residuals. After differencing the data, the coefficient of determination was generally close to zero. There were periods showing correlated short-term variation in GCC and GPP_{max}, for example, at Kaamanen from late May to mid-June in 2016 and in June 2017 (Supplementary materialAppendices Fig. A9–S21e), but most of the common variation in GPP_{max} and GCC was associated with the common seasonal cycle (Table 45).

Table 45: The coefficient of determination (R^2) of the linear regression between GCC and GPP_{max} and of the regression after differencing the data for autocorrelation. Letters a and b refer to the period before and after the annual GCC maximum, respectively.

	Halssiaapa		Lompolojänkkä		Kaamanen	
		Autocorr.		Autocorr.		Autocorr.
	Original R^2	corr. R^2	Original R^2	corr. R^2	Original R^2	corr. R^2
2015 a	0.9749	0.0291	0.9549	0.0055	0.9372	0.0002
2015 b	0.9305	0.0015	0.9697	0.0082	0.9134	0.0023
2016 a	0.9848	0.0020	0.8668	0.1096	0.9304	0.0002
2016 b	0.9660	0.0112	0.9686	0.0001	0.8749	0.0001
2017 a	0.9448	0.0133	0.9599	0.3100	0.9171	0.0195
2017 b	0.9634	0.0550	0.9697	0.0138	0.9724	0.0065
2018 a	0.4468	0.0860	0.8890	0.1413	0.8944	0.0101
2018 b	0.9388	0.0088	0.9840	0.0119	0.9029	0.0045
2019 a	0.8513	0.0473	0.9162	0.0124	0.9854	0.1621
2019 b	0.8198	0.0024	0.9621	0.0011	0.9394	0.0570

3.4 Comparison between digital camera- and satellite-derived GCC

The GCC retrieved GCC from the Sentinel-2 images had the same seasonal pattern as the camera-derived GCC (Fig. 910). Due to the sparseness of satellite data, however, the uncertainties were greater, as shown by the wider confidence intervals. The later season start and GCC maximum in 2017 at all sites and the lower GCC at Halssiaapa in 2018, compared to the other measurement years that were observed with cameras, were visible in the satellite-derived GCC. The GCC values from Sentinel-2 were in general higher than the camera-based GCC, which is most probably due to the different viewing angles and atmospheric effect (the

 scattering and absorption of radiation due to atmospheric molecules and aerosols) and the consequent atmospheric correction of the satellite data.
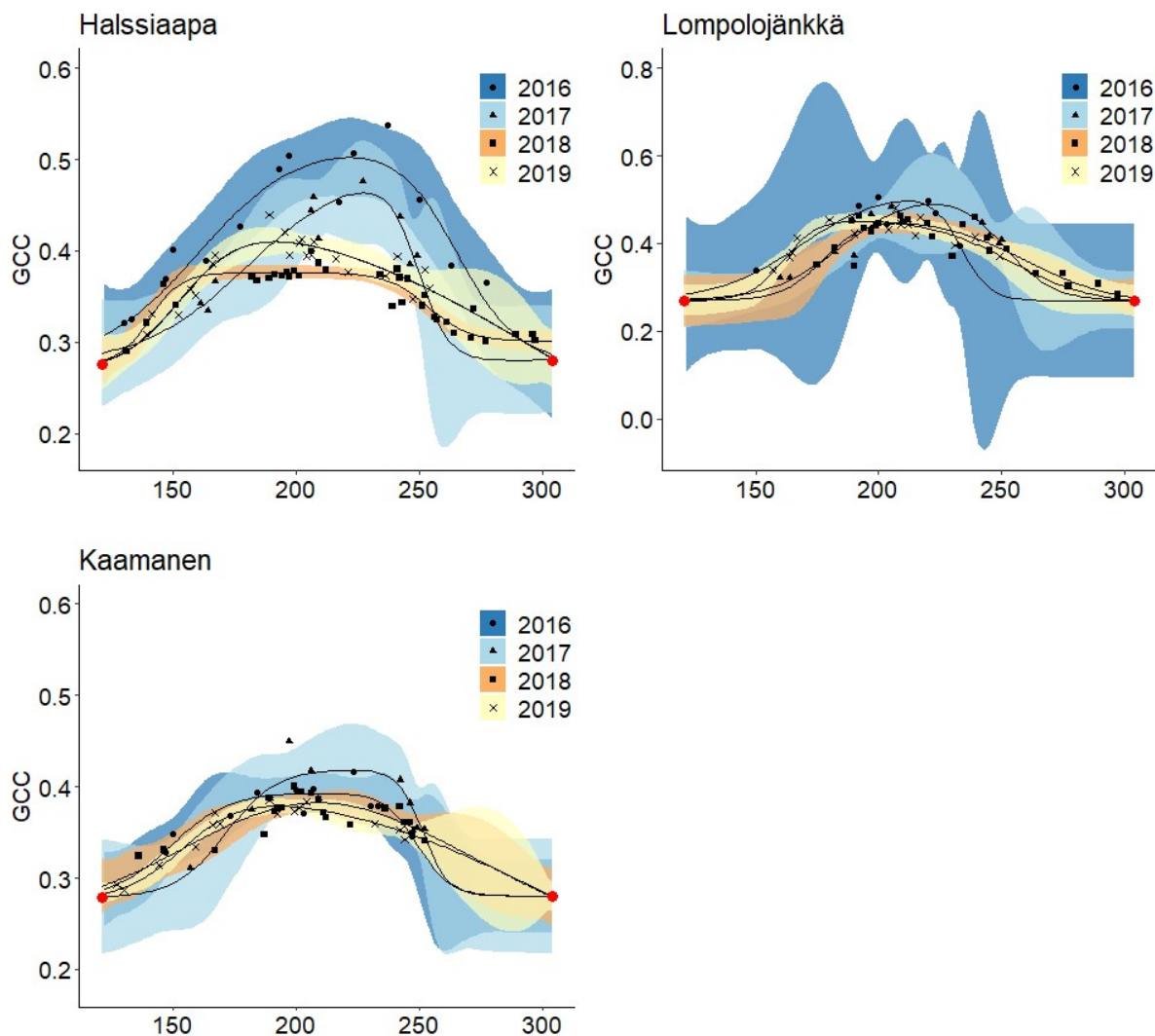
Figure 910: Mean GCC derived from the Sentinel-2 data from 1 May to 30 September in 2016–2019 at Halssiaapa, Lompolojänkkä and Kaamanen. Different symbols and colours denote different years, and the bands show the 95 % confidence intervals of the fitted double hyperbolic tangent function. The red dots indicate the fixed start and end days defined for the fitting. Note the different y-axis scaling for Lompolojänkkä.

The estimated parameters describing different growing season phases, which were calculated from the fitted models, Eq. (2), show substantial differences between satellite and camera data (Table 46). At Halssiaapa and Kaamanen, the season start (SOS25) was estimated to start earlier based on the Sentinel-2 data, whereas at Lompolojänkkä the timing of SOS25 and MAX occurred later. The timing of the end of season (EOS25) was estimated later with the Sentinel-2 data at Halssiaapa and Kaamanen, while at Lompolojänkkä there was no systematic difference.

380 **Table 56: Growing season phases estimated from camera and satellite images (DOY): SOS25 (Start of season, 25 % difference between start and maximum), MAX (maximum GCC) and EOS (End of season, 25 % difference between end and maximum).**

Halssiaapa

	SOS25			Max			EOS25	
	Camera	Satellite		Camera	Satellite		Camera	Satellite
2015	157		2015	208		2015	257	
2016	150	145	2016	197	222	2016	249	280
2017	170	157	2017	215	227	2017	251	258
2018	157	133	2018	212	191	2018	250	265
2019	152	139	2019	192	191	2019	265	288

Lompolojänkkä

	SOS25			Max			EOS25	
	Camera	Satellite		Camera	Satellite		Camera	Satellite
2015	157		2015	202		2015	258	
2016	147	151	2016	193	211	2016	255	241
2017	168	167	2017	204	222	2017	264	265
2018	153	166	2018	196	208	2018	257	279
2019	149	152	2019	182	193	2019	274	273

Kaamanen

	SOS25			Max			EOS25	
	Camera	Satellite		Camera	Satellite		Camera	Satellite
2015	153		2015	213		2015	255	
2016	147	139	2016	198	210	2016	250	258
2017	166	160	2017	211	222	2017	255	258
2018	149	139	2018	207	209	2018	253	288
2019	151	140	2019	201	195	2019	261	288

385 **4 Discussion**

In this study, we examined how vegetation phenology, here described with GCC, varied in three natural peatlands in northern Finland during five growing seasons and how it depends on the site-specific characteristics and the composition of vegetation. The collected data allowed us to create a continuous representation of the development of greenness, which could be related to observed changes in the ecosystem-atmosphere flux of CO_2 and compared with the corresponding satellite-derived data.

390

We found the highest GCC values at Lompolojänkkä, a fen with high nutrient availability, rich vegetation and the highest LAI of the study sites (Fig. 4). The highest GCC also coincided with the highest photosynthetic productivity at peak summer. At Lompolojänkkä, the surface is flatter than at the other sites;, where at Halssiaapa and Kaamanen the pronounced microtopography results in a higher variability in the hydrological features and consequently in the trophic status and vegetation. Also, the stream

395 running through the Lompolojänkkä fen feeds water and nutrients to its surroundings (Lohila et al. 2010, Aurela et al. 2009). This affects the fen's site's nutrient status and is reflected in vegetation, which mainly consists of annuals such as *Carex* spp. and *Menyanthes trifoliata,* and thus in the magnitude of GCC and GPP$_{max}$ reported here.

Related to the microtopographical differences between the study sites, we found a higher GCC in those plant community types that

400   had annuals and taller woody plants with bigger leaves (e.g. *Menyanthes trifoliata*, *Rubus chamaemorus*, *Salix* spp., *Betula* spp.) and, correspondingly, a lower GCC in areas dominated by sedges (e.g. *Carex* spp.) and smaller shrubs (e.g. *Empetrum nigrum*, *Rhododendron tomentusum*, *Andromeda polifolia*) and mosses (Table ~~3~~4, Supplementary material~~Appendices~~ Fig. ~~A1~~S1). At Kaamanen, however, the shrubs (*E. nigrum*, *R. tomentusum*) showed higher GCC than the sedges and mosses. The different plant communities also have different habitats. For example, shrubs ~~thriving~~ thrive in drier locations such as strings, while many annuals

405   (sedges, big-leaved bogbean) favour wetter environment.

Compared to traditional and more laborious measurements of ~~plant growth~~ vegetation phenology, the digital camera-based measurements produce automatically high-frequency data in an effortless way. Even though the variation in GCC among the sites was greater than the variation among~~between~~ the ROIs within one site, our results indicate that vegetation monitoring is feasible

410   even at the plant community level. ~~To our knowledge,~~Comparative studies on the greenness of different plant communities or small ROIs~~have not been defined and compared~~ within ~~from~~ digital camera image~~s with this precision before~~ are still sparse. ~~,~~ For example, Davidson et al. (2021) studied the phenology of different boreal peatland vegetation (defined as bog and fen) at the chamber plot scale (< 0.5 m²), while Menzel et al. (2015) and Cheng et al. (2020) derived vegetation indices from digital images at the scale of individual trees. ~~and we conclude that t~~These kinds of GCC observations of the differentially developing vegetation

415   types have a potential to help decomposing an integrated CO$_2$ flux observation into components allocated to these vegetation types. Different ecosystems, plant communities and species may respond differently to changes in environmental conditions, such as warm spells and timing of the growing season start, depending on their characteristics and habitats.

With regard to timing, ~~A~~a warm spring very likely leads to an earlier growing season start. Nevertheless, even though the growing

420   season start was late at the study sites in 2017, due to a cold spring and late snow melt, vegetation was capable of reaching the same maximum GCC level as in other years, at Lompolojänkkä and Kaamanen even attaining the maximum GCC and GPP$_{max}$ observed during the whole study period (Fig. 8 and 9, Table 3~~5~~). A review of Wipf and Rixen (2010) on arctic and alpine ecosystems concluded that a delayed snowmelt and thus a shorter growing season decreases the overall plant productivity of an ecosystem, but it also noted that the effect of snowmelt timing depends on the plant functional type; for example, the growth of

425   forbs increases while the growth of grasses decreases when the snowmelt occurs later. The later phenological phases are most likely controlled by GDDS rather than the timing of the growing season start (Wipf, 2010). Furthermore, the phenology of ~~those~~ plant species ~~which~~that usually start developing earlier after the snowmelt, and the first phenological phases of all plant species, are more sensitive to changes in the snowmelt timing. Our results imply that the northern peatland vegetation is capable of starting the growth quickly after a cold spring, and the vegetation can even increase gross primary production, if the conditions are

430   favourable later during the growing season, as was the case in 2017. This was clearly observed in the magnitude and timing of the maximum GCC. The faster GCC increase and lower temperature sensitivity at Lompolojänkkä than at the other sites are explained by the nutrient status of this fen.

As observed in several studies conducted in different ecosystems (forests, grasslands, crops, peatlands), GPP correlates strongly

435   with the greenness index derived from digital camera images (Richardson et al., 2008; Migliavacca et al., 2011; Keenan et al., 2014; Peichl et al., 2015; Toomey et al., 2015; Linkosalmi et al., 2016; Knox et al., 2017; Järveoja et al., 2018; Peichl et al., 2018; Koebsch et al., 2019). Our results agree with these studies, showing highly similar seasonal cycles of GCC and GPP$_{max}$ at open

peatlands dominated by shrubs and deciduous plants. Essentially, both are controlled by the amount of green leaf area, which in turn is driven mainly by temperature and day length (Bauerle et al., 2012; Peichl et al., 2015; Koebsch et al., 2019). When temperature increases, the plant chemical reaction rates also increase, triggering photosynthesis (Bonan, 2015). According to our results, air temperature, expressed here as a degree day sum (Fig. 5), explained well the annual differences in the early phase of the growing season, which has also been previously observed for a more southern boreal peatland (Peichl et al. 2015). In the latter part of the growing season, the decreasing day length and temperatures strongly drive the gradual degradation of chlorophyll content, which eventually leads to downregulation of photosynthesis and further to leaf fall and winter dormancy (Larcher, 2003; Öquist and Huner, 2003; Bonan, 2015).

~~While t~~The camera-derived GCC data depicted the differences in the phenological ~~courses~~ development between~~during different~~the measurement years ~~are well depicted by GCC~~, and ~~also~~ the variation in the maximum greenness level among the years and sites, and in relation to GPP_{max}, ~~may be assessed~~could be assessed ~~by~~ from the ~~phenocamera-derived~~ GCC data. Lompolojänkkä showed ~~during all the years~~ significantly higher maximum GCC and GPP_{max} than the other sites during all the years (Fig~~s~~. 7~~8 & 8~~, Table ~~2~~3). Also, the maximum GCC and GPP_{max} were found in the same year at all sites. In addition to the seasonal cycles, ~~both~~ GCC and GPP_{max} show distinct periods of correlated short-term variation, which is mainly controlled by abiotic factors, such as temperature and solar radiation (Peichl et al., 2015). For example, the variation in GCC and GPP_{max} was highly similar during the first part of the growing seasons of 2016 and 2017 at Kaamanen (Supplementary material~~Appendices~~ Fig. ~~A9~~S21~~e~~) and during the drought period in 2018 at Halssiaapa (Figs. 7~~ & 8~~, Supplementary material~~Appendices~~ Fig. ~~A6~~S19). At Lompolojänkkä, this widespread drought did not result in a WTD decrease ~~of the water table level~~ (Supplementary material Fig. S2), which was due to the local hydrological features, and the net CO_2 uptake even increased in contrast to other northern sites (Rinne et al., 2010). At Kaamanen, however, the drought decreased the CO_2 sink, counterbalancing the gain due to the earlier growing season start in 2018 (Heiskanen et al., 2021). Our data show that the drought in 2018 and 2019, observed in WTD and air temperature data (Supplementary material Fig. S2 and Table S1), affected the CO_2 sink most at Halssiaapa (Fig. ~~8~~7, Supplementary material~~Appendices~~ Fig. ~~A7~~S13). The greenness data, both from the Sentinel-2 satellite and ~~repeat~~ digital photography, are in good accord with these observations of CO_2 flux dynamics (Figs. 7, ~~& 8~~, 9 and 10). Despite the specific periods of correlation, our regression analysis indicates that most of the variation in GPP_{max} can be explained by the common seasonal cycle, rather than the short-term variations of GCC (Table ~~4~~5).

The fitting of a hyperbolic tangent function to GCC data to characterize the basic phenological cycle worked well when data availability was sufficient (Figs. 7, ~~ & 8~~, 9 and 10~~9~~). The effect of poor data coverage is especially evident in the Sentinel-2 data in the beginning and end of the growing season, and also when the camera or the GPP_{max} data were limited, ~~e.g.~~ such as in the early growing season at Halssiaapa in 2018 and at Kaamanen in 2019, resulting in wide confidence intervals of the fit (Figs. 7 and 9). Such data losses obviously compromise the accurate timing of the phenological phases. We also found large differences between the camera- and satellite-derived growing season phases (Table ~~4~~6), the fits to the Sentinel-2 data suggesting a longer growing season at Halssiaapa and Kaamanen. Nevertheless, the main phenological changes during the growing season were visible also in the satellite data. Vrieling et al. (2018) found large differences between the phenological parameters derived from the satellite-based NDVI and camera-based GCC time series, especially in the end of the growing season. They suggested that differences could be explained by the non-photosynthetic vegetation mass, such as dead plant matter, stems and flowers, which in an angled view affects the visibility of the green plant mass in the image. Thus, Vrieling et al. (2018) proposed that camera observations taken at nadir, rather than from an angled view, could produce better correlation between satellite and camera data. Also, it should

be noted that the satellite indices are estimated from surface reflectance, while the camera image analysis applies raw digital numbers that scale with the reflected radiance (Vrieling et al., 2018). Thus, the resulting GCC estimates can be expected to differ between the techniques, as also observed in the present study. ~~Vrieling et al. (2018) found large differences between the phenological parameters derived from the satellite based NDVI and camera based GCC time series, especially in the end of the growing season. The differences could be explained by the non-photosynthetic vegetation mass, such as dead plant matter, stems and flowers, which in an angled view affects the visibility of the green plant mass in the image. Thus, Vrieling et al. (2018) suggested that camera observations taken at nadir, rather than from an angled view, could produce better correlation between satellite and camera data. Also, it should be noted that the satellite indices are estimated from surface reflectance, while the camera image analysis applies raw digital numbers that scale with the reflected radiance (Vrieling et al., 2018). Thus, the resulting GCC estimates can be expected to differ between the techniques, as also shown by the present study.~~

Obviously, the temporal coverage of ~~non-cloudy~~ satellite data, typically including ~~an~~non-cloudy image every 5 to 10 days for our study sites, is limited compared to the high-frequency camera-based measurements. The satellite data were limited especially during 2016 and 2017, because at that time Sentinel-2 constellation ~~(Sentinel-2A and Sentinel-2B)~~ consisted only of Sentinel-2A. Since 2018, however, there have been data available from two satellites (Sentinel-2A and Sentinel-2B). Overall, mapping the vegetation on these heterogeneous peatlands with remote sensing methods is challenging and the suitability of the methods depends on the peatland structure (Räsänen et al., 2019). By providing local, continuous data even on the plant community level, digital photography could be used for verification of remote sensing products and as supporting information for their interpretation, as well as for filling the gaps in the landscape-level data (Filippa et al., 2018; Richardson et al., 2007; Richardson et al., 2009; Sonnentag et al., 2012). The applicability of satellite-based remote sensing in tracking vegetation phenology can be improved by increasing the temporal resolution by combining multiple satellite data sources and using data from satellite constellations with very high temporal resolution such as PlanetScope (Cheng et al., 2020; Wand et al., 2020).

5 Conclusions

In this study, we showed that the digital photography derived greenness index (GCC) differed between three northern boreal peatland sites, the differences being associated with nutrient availability and LAI. At all sites, the seasonal course of GCC was closely correlated with that of CO_2 uptake. The digital images also enabled determining the GCC of different plant communities, suggesting that these images can potentially be used for partitioning the ecosystem-scale CO_2 flux measurement. The spring temperatures and consequent variation in growing season start affected the daily GCC and maximum gross photosynthetic production (GPP_{max}~~,~~), but the peatland vegetation showed capability to compensate for a late start, and even to reach the maximum ~~growth level~~GPP_{max} observed during the five study years. The effect of drought on GCC and GPP_{max} depends on local hydrological features and thus the drought resistance of the site, which indicates the possible effects of climate warming and more frequent droughts. Despite the seasonal coherence between the GCC and ~~GPP_{max}~~CO_2 uptake data, the short-term variation of GCC did not in general explain the corresponding variation in GPP_{max}.

The remote sensing (Sentinel-2) data were consistent with the camera-based ~~results~~data, but ~~more satellite data~~ better temporal resolution would be needed for a more reliable timing of different phenological phases. From our analysis of the camera-based results, we can conclude that the chromatic data obtained from digital cameras provide an effective and reliable measurement of vegetation greenness. These observations on vegetation phenology serve as a means of continuous monitoring and understanding

the shifts in vegetation due to land-use and climate change, even on a plant community scale. Time-lapse imaging was here employed in parallel with continuous, ecosystem-scale CO_2 flux measurements, but focused on a small spatial scale it is likely to provide substantial support to non-continuous, chamber-based flux measurements as well. Also, ecosystem modelling could benefit from the parameterization of phenological events based on camera data and the use of these data for model evaluation. Furthermore,

520   these results provide material for the development of dedicated phenology models that can be incorporated into ecosystem models. Finally, we conclude that the digital photography data could be used for verification, interpretation and gap-filling of the remote sensing data.

Appendices

525   Figure A1: The GCC of the different Region of Interests (ROIs) of specific plant communities. The numbers 1-5 indicate the different plant communities detailed in Table 1.

Table A1: The significant differences between different plant communities. The numbers 1-5 indicate the different plant communities detailed in Table 1. For interpretation, a denotes significant (p < 0.05) difference from ROI1, b denotes

530   significant difference from ROI2, c denotes significant difference from ROI3, d denotes significant difference from ROI4 and e denotes significant difference from ROI5.

Figure A2: Daily mean temperatures (°C) and water table depths (cm) in 2015–2019 at the experimental sites.

535   Figure A3: The growing degree days (GDDS) in 2015–2019 at the experimental sites.

Figure A4 a: The normalized cumulative GCC and growing degree days (GDDS) in 2015–2019 at the experimental sites.

Figure A4 b: The normalized cumulative GCC and growing degree days (GDDS) in 2015–2019 at the experimental sites.

540   The data from 2019 is missing.

Figure A4 c: The normalized cumulative GCC and growing degree days (GDDS) in 2015–2019 at the experimental sites.

Figure A5 a: Mean three-day difference in GCC divided to temperature classes (<5 °C, 5-10 °C, >10 °C) at Halssiaapa from May to September. No temperature data in class <5 °C from July and August. The error bars denote the standard error.

545

Figure A5 b: Mean three-day difference in GCC divided to temperature classes (<5 °C, 5-10 °C, >10 °C) at Lompolojänkkä from May to September. No temperature data in class <5 °C from July and August. The error bars denote the standard error.

550   Figure A5 c: Mean three-day difference in GCC divided to temperature classes (<5 °C, 5-10 °C, >10 °C) at Kaamanen from May to September. No temperature data in class <5 °C from July and August. The error bars denote the standard error.

Figure A6 a: The GCC values and fitted function with 95% confidence intervals in 2015–2019 at Halssiaapa. The red dots stand for the fixed start and end point of time in the fitting.

555

Figure A6 b: The GCC values and fitted function with 95% confidence intervals in 2015 – 2019 at Lomoplojänkkä. The red dots stand for the fixed start and end point of time in the fitting.

Figure A6 c: The GCC values and fitted function with 95% confidence intervals in 2015 – 2019 at Kaamanen. The red dots stand for the fixed start and end point of time in the fitting.

560

Figure A7 a: The GPP$_{max}$ values and fitted function with 95% confidence intervals in 2015 – 2019 at Halssiaapa. Note the different scale in 2018. The red dots stand for the fixed start and end point of time in the fitting.

565

Figure A7 b: The GPP$_{max}$ values and fitted function with 95% confidence intervals in 2015 – 2019 at Lompolojänkkä. The red dots stand for the fixed start and end point of time in the fitting.

Figure A7 c: The GPP$_{max}$ values and fitted function with 95% confidence intervals in 2015 – 2019 at Kaamanen. The red dots stand for the fixed start and end point of time in the fitting.

570

Figure A8 a: The regression between GCC and GPP$_{max}$ at Halssiaapa in 2015–2019. The first part of the growing season is denoted with black circles, the latter half with red circles.

Figure A8 b: The regression between GCC and GPP$_{max}$ at Lompoljänkkä in 2015–2019. The first part of the growing season is denoted with black circles, the latter half with red circles.

575

Figure A8 c: The regression between GCC and GPP$_{max}$ at Kaamanen in 2015–2019. The first part of the growing season is denoted with black circles, the latter half with red circles.

Figure A9 a: The scaled GCC and GPP$_{max}$ data at Halssiaapa in 2015–2019.

580

Figure A9 b: The scaled GCC and GPP$_{max}$ data at Lompolojänkkä in 2015–2019.

Figure A9 c: The scaled GCC and GPP$_{max}$ data at Kaamanen in 2015–2019.

Figure A10 a: The Sentinel 2 derived GCC values and fitted function with 95% confidence intervals in 2016 – 2019 at Halssiaapa. The red dots stand for the fixed start and end point of time in the fitting.

585

Figure A10 b: The Sentinel 2 derived GCC values and fitted function with 95% confidence intervals in 2016 – 2019 at Lompolojänkkä. The red dots stand for the fixed start and end point of time in the fitting.

Figure A10 c: The Sentinel 2 derived GCC values and fitted function with 95% confidence intervals in 2016 – 2019 at Kaamanen. The red dots stand for the fixed start and end point of time in the fitting.

590

Author contribution

ANA, MP and TL were responsible for enabling and establishing the camera network. JR, MA and ML set up the digital cameras. AL and MA provided CO_2 measurements and environmental variables. J-PT and MA were responsible for post-processing the CO_2 data. ON performed the satellite (Sentinel-2) data analysis. CMT developed the image processing tool (FMIPROT). ML performed the digital camera image analysis and drafted the manuscript. J-PT, MA and ML and contributed to the interpretation of results and writing on the first version of the manuscript. All authors commented on the manuscript.

Competing interests

The authors declare that they have no conflict of interest.

Acknowledgements

This research has been supported by the Academy of Finland (CAPTURE, grant no. 296888) and the EU (MONIMET Project (LIFE12ENV/FI/000409) funded by EU Life+ Programme 2013–2017).

References

Ahrends, H. E., Etzold, S., Kutsch, W. L., Stoeckli, R., Bruegger, R., Jeanneret, F., Wanner, H., Buchmann, N., and Eugster, W.: Tree phenology and carbon dioxide fluxes: use of digital photography for process-based interpretation at the ecosystem scale, 39, 261–274, https://doi.org/10.3354/cr00811, 2009.

Aurela, M., Tuovinen, J.-P., and Laurila, T.: Carbon dioxide exchange in a subarctic peatland ecosystem in northern Europe measured by the eddy covariance technique, Journal of Geophysical Research: Atmospheres, 103, 11289–11301, https://doi.org/10.1029/98JD00481, 1998.

Aurela, M., Tuovinen, J.-P., and Laurila, T.: Net CO2 exchange of subarctic mountain birch ecosystem, 70, 135–148, https://doi.org/10.1007/s007040170011, 2001.

Aurela, M., Lohila, A., Tuovinen, J.-P., Hatakka, J., Riutta, T., and Laurila, T.: Carbon dioxide exchange on a northern boreal fen, 14, 699–710, 2009.

Barr, A. G., Black, T. A., Hogg, E. H., GRIFFIS, T. J., Morgenstern, K., Kljun, N., Theede, A., and Nesic, Z.: Climatic controls on the carbon and water balances of a boreal aspen forest, 1994–2003, Global Change Biology, 13, 561–576, https://doi.org/10.1111/j.1365-2486.2006.01220.x, 2007.

Bauerle, W. L., Oren, R., Way, D. A., Qian, S. S., Stoy, P. C., Thornton, P. E., Bowden, J. D., Hoffman, F. M., and Reynolds, R. F.: Photoperiodic regulation of the seasonal pattern of photosynthetic capacity and the implications for carbon cycling, Proc Natl Acad Sci USA, 109, 8612, https://doi.org/10.1073/pnas.1119131109, 2012.

Berninger, F.: Effects of Drought and Phenology on GPP in Pinus sylvestris: A Simulation Study Along a Geographical Gradient, 11, 33–42, 1997.

Black, T. A., Chen, W. J., Barr, A. G., Arain, M. A., Chen, Z., Nesic, Z., Hogg, E. H., Neumann, H. H., and Yang, P. C.: Increased carbon sequestration by a boreal deciduous forest in years with a warm spring, Geophysical Research Letters, 27, 1271–1274, https://doi.org/10.1029/1999GL011234, 2000.

Bonan, G.: Ecological Climatology: Concepts and Applications, 3rd ed., Cambridge University Press, Cambridge, https://doi.org/10.1017/CBO9781107339200, 2015.

Bryant, R. G. and Baird, A. J.: The spectral behaviour of Sphagnum canopies under varying hydrological conditions, Geophysical Research Letters, 30, https://doi.org/10.1029/2002GL016053, 2003.

Cheng, Y., Vrieling, A., Fava, F., Meroni, M., Marshall, M., and Gachoki, S.: Phenology of short vegetation cycles in a Kenyan rangeland from PlanetScope and Sentinel-2, Remote Sensing of Environment, 248, 112004, https://doi.org/10.1016/j.rse.2020.112004, 2020.

Crowther, T. W., Todd-Brown, K. E. O., Rowe, C. W., Wieder, W. R., Carey, J. C., Machmuller, M. B., Snoek, B. L., Fang, S., Zhou, G., Allison, S. D., Blair, J. M., Bridgham, S. D., Burton, A. J., Carrillo, Y., Reich, P. B., Clark, J. S., Classen, A. T., Dijkstra, F. A., Elberling, B., Emmett, B. A., Estiarte, M., Frey, S. D., Guo, J., Harte, J., Jiang, L., Johnson, B. R., Kröel-Dulay, G., Larsen, K. S., Laudon, H., Lavallee, J. M., Luo, Y., Lupascu, M., Ma, L. N., Marhan, S., Michelsen, A., Mohan, J., Niu, S., Pendall, E., Peñuelas, J., Pfeifer-Meister, L., Poll, C., Reinsch, S., Reynolds, L. L., Schmidt, I. K., Sistla, S., Sokol, N. W., Templer, P. H., Treseder, K. K., Welker, J. M., and Bradford, M. A.: Quantifying global soil carbon losses in response to warming, Nature, 540, 104–108, https://doi.org/10.1038/nature20150, 2016.

Davidson, S. J., Goud, E. M., Malhotra, A., Estey, C. O., Korsah, P., and Strack, M.: Linear Disturbances Shift Boreal Peatland Plant Communities Toward Earlier Peak Greenness, Journal of Geophysical Research: Biogeosciences, 126, e2021JG006403, https://doi.org/10.1029/2021JG006403, 2021.

Delbart, N., Picard, G., Le Toan, T., Kergoat, L., Quegan, S., Woodward, I., Dye, D., and Fedotova, V.: Spring phenology in boreal Eurasia over a nearly century time scale, Global Change Biology, 14, 603–614, https://doi.org/10.1111/j.1365-2486.2007.01505.x, 2008.

Dunn, A. L., Barford, C. C., Wofsy, S. C., Goulden, M. L., and Daube, B. C.: A long-term record of carbon exchange in a boreal black spruce forest: means, responses to interannual variability, and decadal trends, Global Change Biology, 13, 577–590, https://doi.org/10.1111/j.1365-2486.2006.01221.x, 2007.

Filippa, G., Cremonese, E., Migliavacca, M., Galvagno, M., Sonnentag, O., Humphreys, E., Hufkens, K., Ryu, Y., Verfaillie, J., Morra di Cella, U., and Richardson, A. D.: NDVI derived from near-infrared-enabled digital cameras: Applicability across different plant functional types, Agricultural and Forest Meteorology, 249, 275–285, https://doi.org/10.1016/j.agrformet.2017.11.003, 2018.

650 Gorham, E.: Northern Peatlands: Role in the Carbon Cycle and Probable Responses to Climatic Warming, Ecological Applications, 1, 182–195, https://doi.org/10.2307/1941811, 1991.

Goulden, M. L., Munger, J. W., Fan, S.-M., Daube, B. C., and Wofsy, S. C.: Measurements of carbon sequestration by long-term eddy covariance: methods and a critical evaluation of accuracy, Global Change Biology, 2, 169–182, https://doi.org/10.1111/j.1365-2486.1996.tb00070.x, 1996.

655 Harenda, K. M., Lamentowicz, M., Samson, M., and Chojnicki, B. H.: The Role of Peatlands and Their Carbon Storage Function in the Context of Climate Change, in: Interdisciplinary Approaches for Sustainable Development Goals: Economic Growth, Social Inclusion and Environmental Protection, edited by: Zielinski, T., Sagan, I., and Surosz, W., Springer International Publishing, Cham, 169–187, https://doi.org/10.1007/978-3-319-71788-3_12, 2018.

Heiskanen, L., Tuovinen, J.-P., Räsänen, A., Virtanen, T., Juutinen, S., Lohila, A., Penttilä, T., Linkosalmi, M., Mikola, J., Laurila, 660 T., and Aurela, M.: Carbon dioxide and methane exchange of a patterned subarctic fen during two contrasting growing seasons, 18, 873–896, https://doi.org/10.5194/bg-18-873-2021, 2021.

Ide, R. and Oguma, H.: Use of digital cameras for phenological observations, Ecological Informatics, 5, 339–347, https://doi.org/10.1016/j.ecoinf.2010.07.002, 2010.

Järveoja, J., Nilsson, M. B., Gažovič, M., Crill, P. M., and Peichl, M.: Partitioning of the net CO2 exchange using an automated 665 chamber system reveals plant phenology as key control of production and respiration fluxes in a boreal peatland, Global Change Biology, 24, 3436–3451, https://doi.org/10.1111/gcb.14292, 2018.

Keeling, C. D., Chin, J. F. S., and Whorf, T. P.: Increased activity of northern vegetation inferred from atmospheric CO2 measurements, Nature, 382, 146–149, https://doi.org/10.1038/382146a0, 1996.

Keenan, T. F., Gray, J., Friedl, M. A., Toomey, M., Bohrer, G., Hollinger, D. Y., Munger, J. W., O'Keefe, J., Schmid, H. P., Wing, 670 I. S., Yang, B., and Richardson, A. D.: Net carbon uptake has increased through warming-induced changes in temperate forest phenology, Nature Climate Change, 4, 598–604, https://doi.org/10.1038/nclimate2253, 2014.

Knox, S. H., Dronova, I., Sturtevant, C., Oikawa, P. Y., Matthes, J. H., Verfaillie, J., and Baldocchi, D.: Using digital camera and Landsat imagery with eddy covariance data to model gross primary production in restored wetlands, Agricultural and Forest Meteorology, 237–238, 233–245, https://doi.org/10.1016/j.agrformet.2017.02.020, 2017.

675 Koebsch, F., Sonnentag, O., Järveoja, J., Peltoniemi, M., Alekseychik, P., Aurela, M., Arslan, A. N., Dinsmore, K., Gianelle, D., Helfter, C., Jackowicz-Korczynski, M., Korrensalo, A., Leith, F., Linkosalmi, M., Lohila, A., Lund, M., Maddison, M., Mammarella, I., Mander, Ü., Minkkinen, K., Pickard, A., Pullens, J. W. M., Tuittila, E.-S., Nilsson, M. B., and Peichl, M.: Refining the role of phenology in regulating gross ecosystem productivity across European peatlands, Global Change Biology, 26, 876–887, https://doi.org/10.1111/gcb.14905, 2020.

680 Körner Christian and Basler David: Phenology Under Global Warming, Science, 327, 1461–1462, https://doi.org/10.1126/science.1186473, 2010.

Larcher, W., Huber-Sannwald, E., and Wieser, J.: Physiological Plant Ecology: Ecophysiology and Stress Physiology of Functional Groups, Springer, 2003.

Lehtonen, I. and Pirinen, P.: 2018: An exceptionally warm thermal growing season in Finland, 1, https://doi.org/10.35614/ISSN-685 2341-6408-IK-2019-03-RL, 2019.

Lees, K. J., Quaife, T., Artz, R. R. E., Khomik, M., and Clark, J. M.: Potential for using remote sensing to estimate carbon fluxes across northern peatlands – A review, Science of The Total Environment, 615, 857–874, https://doi.org/10.1016/j.scitotenv.2017.09.103, 2018.

Linkosalmi, M., Aurela, M.-, Tuovinen, J.-P., Peltoniemi, M., Tanis, C. M., Arslan, A. N., Kolari, P., Böttcher, K., Aalto, T., 690 Rainne, J., Hatakka, J., and Laurila, T.: Digital photography for assessing the link between vegetation phenology and CO2 exchange in two contrasting northern ecosystems, 5, 417–426, https://doi.org/10.5194/gi-5-417-2016, 2016.

Linkosalo, T., Häkkinen, R., Terhivuo, J., Tuomenvirta, H., and Hari, P.: The time series of flowering and leaf bud burst of boreal trees (1846–2005) support the direct temperature observations of climatic warming, Agricultural and Forest Meteorology, 149, 453–461, https://doi.org/10.1016/j.agrformet.2008.09.006, 2009.

695 Lohila, A., Aurela, M., Hatakka, J., Pihlatie, M., Minkkinen, K., Penttilä, T., and Laurila, T.: Responses of N2O fluxes to temperature, water table and N deposition in a northern boreal fen, European Journal of Soil Science, 61, 651–661, https://doi.org/10.1111/j.1365-2389.2010.01265.x, 2010.

Lund, M., Christensen, T. R., Lindroth, A., and Schubert, P.: Effects of drought conditions on the carbon dioxide dynamics in a temperate peatland, 7, https://doi.org/10.1088/1748-9326/7/4/045704, 2012.

700 Maanavilja, L., Riutta, T., Aurela, M., Pulkkinen, M., Laurila, T., and Tuittila, E.-S.: Spatial variation in CO2 exchange at a northern aapa mire, Biogeochemistry, 104, 325–345, https://doi.org/10.1007/s10533-010-9505-7, 2011.

Menzel, A., Helm, R., and Zang, C.: Patterns of late spring frost leaf damage and recovery in a European beech (Fagus sylvatica L.) stand in south-eastern Germany based on repeated digital photographs, Frontiers in Plant Science, 6, 2015.

Meroni, M., Verstraete, M. M., Rembold, F., Urbano, F., and Kayitakire, F.: A phenology-based method to derive biomass
705 production anomalies for food security monitoring in the Horn of Africa, null, 35, 2472–2492, https://doi.org/10.1080/01431161.2014.883090, 2014.

Migliavacca, M., Galvagno, M., Cremonese, E., Rossini, M., Meroni, M., Sonnentag, O., Cogliati, S., Manca, G., Diotri, F., Busetto, L., Cescatti, A., Colombo, R., Fava, F., Morra di Cella, U., Pari, E., Siniscalco, C., and Richardson, A. D.: Using digital repeat photography and eddy covariance data to model grassland phenology and photosynthetic CO2 uptake, Agricultural and
710 Forest Meteorology, 151, 1325–1337, https://doi.org/10.1016/j.agrformet.2011.05.012, 2011.

Migliavacca, M., Sonnentag, O., Keenan, T. F., Cescatti, A., O'Keefe, J., and Richardson, A. D.: On the uncertainty of phenological responses to climate change, and implications for a terrestrial biosphere model, 9, 2063–2083, https://doi.org/10.5194/bg-9-2063-2012, 2012.

Morisette, J. T., Richardson, A. D., Knapp, A. K., Fisher, J. I., Graham, E. A., Abatzoglou, J., Wilson, B. E., Breshears, D. D.,
715 Henebry, G. M., Hanes, J. M., and Liang, L.: Tracking the Rhythm of the Seasons in the Face of Global Change: Phenological Research in the 21st Century, 7, 253–260, 2009.

Nordli, Ø., Wielgolaski, F. E., Bakken, A. K., Hjeltnes, S. H., Måge, F., Sivle, A., and Skre, O.: Regional trends for bud burst and flowering of woody plants in Norway as related to climate change, International Journal of Biometeorology, 52, 625–639, https://doi.org/10.1007/s00484-008-0156-5, 2008.

720 Öquist, G. and Huner, N. P. A.: Photosynthesis of Overwintering Evergreen Plants, Annu. Rev. Plant Biol., 54, 329–355, https://doi.org/10.1146/annurev.arplant.54.072402.115741, 2003.

Peichl, M., Sonnentag, O., and Nilsson, M. B.: Bringing Color into the Picture: Using Digital Repeat Photography to Investigate Phenology Controls of the Carbon Dioxide Exchange in a Boreal Mire, Ecosystems, 18, 115–131, https://doi.org/10.1007/s10021-014-9815-z, 2015.

725 Peichl, M., Gažovič, M., Vermeij, I., de Goede, E., Sonnentag, O., Limpens, J., and Nilsson, M. B.: Peatland vegetation composition and phenology drive the seasonal trajectory of maximum gross primary production, Scientific Reports, 8, 8012, https://doi.org/10.1038/s41598-018-26147-4, 2018.

Peltoniemi, M., Aurela, M., Böttcher, K., Kolari, P., Loehr, J., Karhu, J., Linkosalmi, M., Tanis, C. M., Tuovinen, J.-P., and Arslan, A. N.: Webcam network and image database for studies of phenological changes of vegetation and snow cover in Finland, image
730 time series from 2014 to 2016, 10, 173–184, https://doi.org/10.5194/essd-10-173-2018, 2018.

Pudas, E., Leppälä, M., Tolvanen, A., Poikolainen, J., Venäläinen, A., and Kubin, E.: Trends in phenology of Betula pubescens across the boreal zone in Finland, International Journal of Biometeorology, 52, 251–259, https://doi.org/10.1007/s00484-007-0126-3, 2008.

Räsänen, A., Aurela, M., Juutinen, S., Kumpula, T., Lohila, A., Penttilä, T., and Virtanen, T.: Detecting northern peatland
735 vegetation patterns at ultra-high spatial resolution, Remote Sensing in Ecology and Conservation, 6, 457–471, https://doi.org/10.1002/rse2.140, 2020.

Richardson, A. D., Jenkins, J. P., Braswell, B. H., Hollinger, D. Y., Ollinger, S. V., and Smith, M.-L.: Use of digital webcam images to track spring green-up in a deciduous broadleaf forest, Oecologia, 152, 323–334, https://doi.org/10.1007/s00442-006-0657-z, 2007.

740 Richardson, A. D., Hollinger, D. Y., Dail, D. B., Lee, J. T., Munger, J. W., and O'Keefe, J.: Influence of spring phenology on seasonal and annual carbon balance in two contrasting New England forests, Tree Physiology, 29, 321–331, 2009.

Richardson, A. D., Keenan, T. F., Migliavacca, M., Ryu, Y., Sonnentag, O., and Toomey, M.: Climate change, phenology, and phenological control of vegetation feedbacks to the climate system, Agricultural and Forest Meteorology, 169, 156–173, https://doi.org/10.1016/j.agrformet.2012.09.012, 2013.

745 Richardson, A. D.: Tracking seasonal rhythms of plants in diverse ecosystems with digital camera imagery, New Phytologist, 222, 1742–1750, https://doi.org/10.1111/nph.15591, 2019.

Rinne, J., Tuovinen, J.-P., Klemedtsson, L., Aurela, M., Holst, J., Lohila, A., Weslien, P., Vestin, P., Łakomiec, P., Peichl, M., Tuittila, E.-S., Heiskanen, L., Laurila, T., Li, X., Alekseychik, P., Mammarella, I., Ström, L., Crill, P., and Nilsson, M. B.: Effect of the 2018 European drought on methane and carbon dioxide exchange of northern mire ecosystems, Philosophical Transactions
750 of the Royal Society B: Biological Sciences, 375, 20190517, https://doi.org/10.1098/rstb.2019.0517, 2020.

Sonnentag, O., Chen, J. M., Roberts, D. A., Talbot, J., Halligan, K., and Govind, A.: Mapping tree and shrub leaf area indices in an ombrotrophic peatland through multiple endmember spectral unmixing, 109, 342–360, https://doi.org/10.1016/j.rse.2007.01.010, 2007.

Sonnentag, O., Detto, M., Vargas, R., Ryu, Y., Runkle, B. R. K., Kelly, M., and Baldocchi, D. D.: Tracking the structural and
755 functional development of a perennial pepperweed (Lepidium latifolium L.) infestation using a multi-year archive of webcam imagery and eddy covariance measurements, Agricultural and Forest Meteorology, 151, 916–926, https://doi.org/10.1016/j.agrformet.2011.02.011, 2011.

Sonnentag, O., Hufkens, K., Teshera-Sterne, C., Young, A. M., Friedl, M., Braswell, B. H., Milliman, T., O'Keefe, J., and Richardson, A. D.: Digital repeat photography for phenological research in forest ecosystems, Agricultural and Forest
760 Meteorology, 152, 159–177, https://doi.org/10.1016/j.agrformet.2011.09.009, 2012.

Tanis, C. M., Peltoniemi, M., Linkosalmi, M., Aurela, M., Böttcher, K., Manninen, T., and Arslan, A. N.: A System for Acquisition, Processing and Visualization of Image Time Series from Multiple Camera Networks, 3, https://doi.org/10.3390/data3030023, 2018.

Toomey, M., Friedl, M. A., Frolking, S., Hufkens, K., Klosterman, S., Sonnentag, O., Baldocchi, D. D., Bernacchi, C. J., Biraud,
765 S. C., Bohrer, G., Brzostek, E., Burns, S. P., Coursolle, C., Hollinger, D. Y., Margolis, H. A., McCaughey, H., Monson, R. K., Munger, J. W., Pallardy, S., Phillips, R. P., Torn, M. S., Wharton, S., Zeri, M., and Richardson, A. D.: Greenness indices from digital cameras predict the timing and seasonal dynamics of canopy-scale photosynthesis, Ecological Applications, 25, 99–115, https://doi.org/10.1890/14-0005.1, 2015.

Turunen, J., Tomppo, E., Tolonen, K., and Reinikainen, A.: Estimating carbon accumulation rates of undrained mires in Finland–
770 application to boreal and subarctic regions, The Holocene, 12, 69–80, https://doi.org/10.1191/0959683602hl522rp, 2002.

Vrieling, A., Meroni, M., Darvishzadeh, R., Skidmore, A. K., Wang, T., Zurita-Milla, R., Oosterbeek, K., O'Connor, B., and Paganini, M.: Vegetation phenology from Sentinel-2 and field cameras for a Dutch barrier island, Remote Sensing of Environment, 215, 517–529, https://doi.org/10.1016/j.rse.2018.03.014, 2018.

White, M. A. and Nemani, R. R.: Canopy duration has little influence on annual carbon storage in the deciduous broad leaf forest,
775 Global Change Biology, 9, 967–972, https://doi.org/10.1046/j.1365-2486.2003.00585.x, 2003.

Wingate, L., Ogée, J., Cremonese, E., Filippa, G., Mizunuma, T., Migliavacca, M., Moisy, C., Wilkinson, M., Moureaux, C., Wohlfahrt, G., Hammerle, A., Hörtnagl, L., Gimeno, C., Porcar-Castell, A., Galvagno, M., Nakaji, T., Morison, J., Kolle, O., Knohl, A., Kutsch, W., Kolari, P., Nikinmaa, E., Ibrom, A., Gielen, B., Eugster, W., Balzarolo, M., Papale, D., Klumpp, K., Köstner, B., Grünwald, T., Joffre, R., Ourcival, J.-M., Hellstrom, M., Lindroth, A., George, C., Longdoz, B., Genty, B., Levula,
780 J., Heinesch, B., Sprintsin, M., Yakir, D., Manise, T., Guyon, D., Ahrends, H., Plaza-Aguilar, A., Guan, J. H., and Grace, J.: Interpreting canopy development and physiology using a European phenology camera network at flux sites, 12, 5995–6015, https://doi.org/10.5194/bg-12-5995-2015, 2015.

Wipf, S.: Phenology, growth, and fecundity of eight subarctic tundra species in response to snowmelt manipulations, Plant Ecology, 207, 53–66, https://doi.org/10.1007/s11258-009-9653-9, 2010.

785   Wipf, S. and Rixen, C.: A review of snow manipulation experiments in Arctic and alpine tundra ecosystems, POLAR, 29, 95–109, https://doi.org/10.3402/polar.v29i1.6054, 2010.